ABSTRACT

SENSITIVITY OF DIFFUSE CORRELATION SPECTROSCOPY TO FLOW RATES IN TISSUE-SIMULATING OPTICAL PHANTOMS

by Sara Marie Zanfardino

This thesis explored diffuse correlation spectroscopy (DCS) as a flow-monitoring technique along with its theoretical formalism and experimental applications. Experimental data as presented here has validated our DCS system as a reliable, optical flow sensing device. The experiments report the decrease in DCS sensitivity to distinguish between flow speeds as the depth of the flow channel increases. The influence of optical properties of the medium surrounding a buried flow channel was investigated. This thesis concludes with the discussion of potential avenues for future research to expand these experiments.

SENSITIVITY OF DIFFUSE CORRELATION SPECTROSCOPY TO FLOW RATES IN TISSUE-SIMULATING OPTICAL PHANTOMS

A Thesis

Submitted to the

Faculty of Miami University

in partial fulfillment of

the requirements for the degree of

Master of Science

by

Sara Marie Zanfardino

Miami University

Oxford, Ohio

2018

Advisor: Dr. Karthik Vishwanath

Reader: Dr. Samir Bali

Reader: Dr. Paul Urayama

This Thesis titled

SENSITIVITY OF DIFFUSE CORRELATION SPECTROSCOPY TO FLOW RATES IN TISSUE-SIMULATING OPTICAL PHANTOMS

by

Sara Marie Zanfardino

has been approved for publication by

The College of Arts and Science

and

Department of Physics

_____

Dr. Karthik Vishwanath

_____

Dr. Samir Bali

_____

Dr. Paul Urayama

TABLE OF CONTENTS

LIST OF TABLES

LIST OF FIGURES

DEDICATION

To my late grandmother. Without her undeniable example of compassion and service to others in which she demonstrated to me each and every day of her life, I would not be the woman I am today. Her support and unwavering faith in my ability to succeed encouraged me to maintain in pursuit of my goals at the toughest of times. The endless hours she spent with me as a child each night helping me with my cursive, double-checking my homework assignments, and running through my math flashcards for quizzes 100 times over demonstrated to me the value of education and how fortunate I am to have experienced education as I have. I hope to serve as such an example and mentor for many other young men and women who come after me and inspire them to appreciate and value education as I have learned to.

ACKNOWLEDGEMENTS

I would like to acknowledge the entire Miami University Department of Physics faculty, staff, family, and friends. Specifically, I would like to thank my advisor, Dr. Karthik Vishwanath, for sharing his expertise in the field of diffuse optics with me. For without his guidance, I would not be here writing this thesis today. I would like to also thank Dr. Christopher Beer for encouraging me to apply to this program. As an introductory physics student in his class with no intention of going to graduate school, let alone graduate school for physics, that seemed like quite a frightening suggestion at the time. I would also like that thank my best friend and roommate, Kamaran Price. Her unwavering support and understanding of my non-stop work schedule that resulted in me never having free time to spend with her encouraged me to keep believing that one day this will all pay off. With a little hard work and a whole lot of faith, everything worked out. Last, but certainly not least, I would also like to thank my family - mom, dad, and sister – for all of their continued support throughout my journey… and also for never questioning why I love school so much.

CHAPTER 1: INTRODUCTION

1.1 Thesis Organization

This thesis will introduce and discuss how light interacts with turbid, or optically dense, media. This will lead into the discussion of how optical methods have been adapted so that by using them, information about properties within the media can be extracted. Specifically, this thesis will focus on how near-infrared (NIR) and coherent light sources in diffuse correlation spectroscopy (DCS) are utilized in conjugation with a fiber optic probe to gain information about relative flow changes occurring in an optically dense media. The evolution of DCS will be introduced by briefly describing its other optical spectroscopic predecessors and provide an overview of the theoretical formalism behind DCS. This thesis will discuss how this theory is implemented in experiments by introducing the hardware that a DCS setup is comprised of. Following the introduction, theory, and experimental setup, a series of experiments that demonstrate the ability of DCS to sense relative changes in flow directed through a channel which is embedded in an optical phantom, a tissue-like medium, will be presented. The motivation as well as the shortcomings and successes of each experiment in additional to the future research that this thesis has laid the foundation for will be discussed.

1.2 Light Interaction with Media

The manner in which light interacts with turbid media is a well-studied phenomenon that has given rise to many divisions of optical research that exist today. As depicted in Figure 1 below, some of the ways in which light can interact with a turbid medium are shown. Light can: 1) undergo specular reflectance which involves like reflecting off the surface of the medium, preventing any light from entering medium, 2) interact with a scattering particle and deflect from one scatter to another in any direction, 3) be transmitted through the medium with or without any interactions before it exits, and 4) be absorbed by an absorbing particle [1-3].

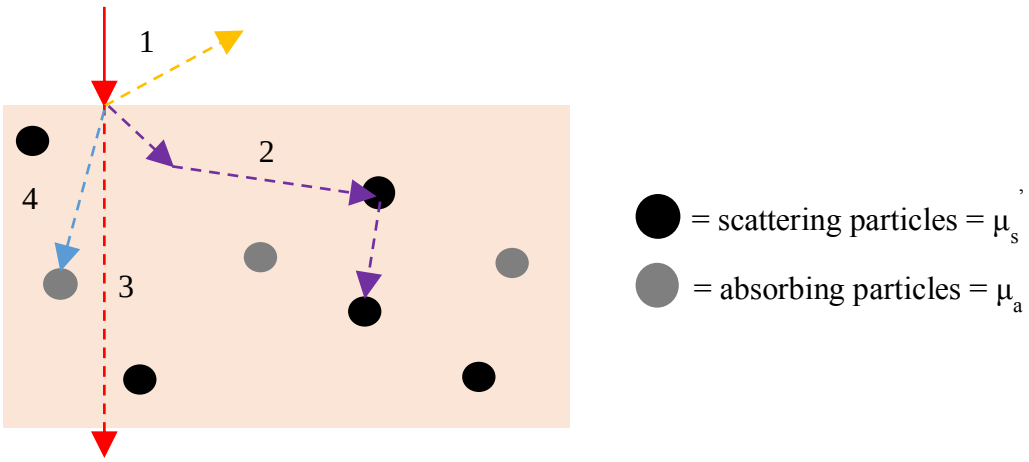

Figure 1: Light interaction with media: 1) specular reflectance, 2) scattering, 3) transmittance, and 4) absorption

Diffuse Correlation Spectroscopy (DCS) has evolved from a series of related spectroscopic techniques, one being Diffuse Light Spectroscopy (DLS). DLS originated as a method of imaging much simpler media where the single-scattering limit is considered valid [4]. In order to study more complex media, such as a tissue sample for instance, a multiple-scattering model (i.e. photons undergoing multiple consecutive scattering events before reaching a detector) was developed and became known as Diffusing Wave Spectroscopy (DWS) [5-7]. DCS later evolved when the notion of diffuse optical transport and its theoretical roots were applied to the foundations of DLS and DWS [8]. Since then, DCS has been utilized to study relative flow rates and various other optical properties of a medium [9-17]. Optical spectroscopic techniques can be used to create a spatial map of optical properties of a turbid sample by measurement of temporal or spatial fluctuations in backscattered light.

The notion of a turbid or optically dense refers to the scattering and absorbing properties of the medium. These optical properties are described by the medium's absorption and scattering coefficients, μ_a and μ_s respectively, and have significant dependence on the wavelength of the incident light. The scattering coefficient is approximated as the reciprocal of the scattering length l_s, which was estimated to be as small as tens of millimeters, while the absorption coefficient is then the reciprocal of the absorption length l_a and can be as large as a few millimeters [18]. Both of these values are estimated for a red blood cell composition of 40% with respect to total blood volume. Biological samples, such as tissues and blood for example, are comprised in large by scattering and absorbing particles, making the study of how light interacts with various tissues of interest to the biomedical community.

This purpose of the experiments presented here was to explore diffuse correlation spectroscopy (DCS) as a flow-monitoring instrument along with its theoretical formalism and experimental implications. The aim of the experiments conducted was to determine how factors, such as the depth of a flow channel and how the optical properties of the medium surrounding the flow channel, affect the DCS system's ability to sense flow.

CHAPTER 2: THE UNNORMALIZED ELECTRIC FIELD AND NORMALIZED INTENSITY AUTOCORRELATION FUNCTIONS

2.1 Theoretical Determination of the Unnormalized Electric Field Autocorrelation Function

Photon transport theory is a well understood theoretical formalism which describes photon propagation though a turbid medium [19]. In photon transport theory, one considers the net change in photon radiance or power density ($W \cdot m^{-2}$) over an infinitely small region, shown outlined in red in Figure 2.

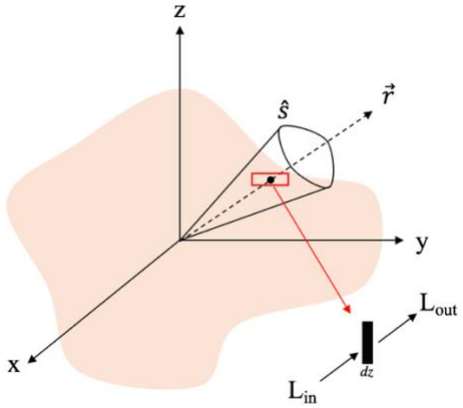

Figure 2: Depiction of region of interest and representation of photon radiance in and out of the designated region of width dz.

In a small "pillbox" region of width *dz* there exists incident radiance (L_{in}) and radiance leaving the region (L_{out}). The net summation of photon radiance must be zero; any photons absorbed by the medium or scattered out of *dz* must be equally matched by photons scattered from another region $\hat{s}$ into *dz* so that $\frac{dL}{dz} = 0$ [20]. This conservation of radiance is illustrated by the radiative transport equation (RTE)

$$\frac{1}{v}\frac{\partial L(\vec{r},\hat{\Omega},t)}{\partial t} + \nabla \cdot L(\vec{\boldsymbol{r}},\hat{\Omega},t)\hat{\Omega} + \mu_t L(\vec{\boldsymbol{r}},\hat{\Omega},\tau) = \mu_s \int d\hat{\Omega}' L(\vec{\boldsymbol{r}},\hat{\Omega}',t) f(\hat{\Omega},\hat{\Omega}') + S(r,\hat{\Omega},t). \quad (1)$$

In the RTE, $\hat{\Omega}' L(\vec{\mathbf{r}},\hat{\Omega}',\mathrm{t})$ describes the radiance at some point in space $\boldsymbol{r}$, traveling in the direction of $\hat{\Omega}'$ at a given time *t* and *v* is the speed of light. The term $f(\hat{\Omega},\hat{\Omega}')$ represents the probability of scattering in direction $\hat{\Omega}'$ from $\hat{\Omega}$, denoted as $\hat{s}$ and *dz* in Figure 2 above. The variable μ_t is equal to the sum of the scattering and absorption coefficients, μ_s and μ_a, respectively. The RTE represents the conservation of energy within a small region surrounding a point in space. The first term on the left-hand side of the equation is equivalent to the net number of photons entering the region in space being examined. The second term represents the flux of photons in *dz*. The third term on the left-hand side of the RTE represents the loss that results from photons scattering out of *dz* or being absorbed in the medium within the region *dz*. On the

right-hand side of the equation, the first term is representative of the photons being scattered into the region of interest from another region outside of *dz* and finally, the last term on the right-hand side of the equation is representative of the source photons reaching the point of interest without being scattered. The RTE is difficult to solve for anything besides an overly simplified geometry, but by applying the P_1 approximation which expands the radiance and probability terms as spherical harmonics, one can integrate the radiance over the solid angle and obtain the photon diffusion equation [8, 20, 21]

$$\left[D_\gamma \nabla^2 - v\mu_a\right]\Phi(\vec{\boldsymbol{r}}, t) = vS(\vec{\boldsymbol{r}}, t). \tag{2}$$

The photon diffusion equation can be solved to provide an analytical expression for the photon fluence $\Phi(\vec{\boldsymbol{r}}, t)$ given as

$$\Phi(\vec{\boldsymbol{r}}, t) = \frac{3\mu_s'}{4\pi}\left(\frac{\exp(-Kr_1)}{r_1} - \frac{\exp(-Kr_2)}{r_2}\right). \tag{3}$$

In the exponential, $K = 3\mu_a\mu_s'$ while $r_1 = [z_0^2 + \rho^2]^{1/2}$ and $r_2 = [(z_0 + 2z_b)^2 + \rho^2]^{1/2}$ where ρ is the distance parallel to the sample boundary, z_0 is the random walk step equivalent to $1/\mu_s'$ and finally z_b is the extrapolated zero boundary, meaning the point in space at which it is taken that the photon fluence is zero. $S(\vec{\boldsymbol{r}}, t)$ is the spatial distribution of the light source at position $\vec{\boldsymbol{r}}$ in space, μ_a is the absorption coefficient [19, 21]. D_γ refers to the photon diffusion coefficient ($D_\gamma = \frac{1}{3(\mu_a + \mu_s')}$ with μ_s' as the reduced scattering coefficient and μ_a as the absorption coefficient). The reduced scattering coefficient is related to the anisotropy function, describing the probability function of forward scattering, $\mu_s' = \mu_s(1 - g)$ where $g = \langle \cos\theta \rangle$ and is typically ~0.9 for tissue samples [22]. In the expression for the anisotropy, θ is the angle measured at the point of deflection from a scattering particle with respect to its initial angle of incidence.

In a similar manner to the RTE, an analytical expression for the unnormalized autocorrelation function $G_1(\vec{\boldsymbol{r}}, \tau)$ can be derived by applying the P_1 approximation to the correlation transport equation (CTE) as written as

$$\nabla \cdot G_1^T(\vec{\boldsymbol{r}}, \hat{\Omega}, \tau)\hat{\Omega} + \mu_t G_1^T(\vec{\boldsymbol{r}}, \hat{\Omega}, \tau) = \mu_s \int d\hat{\Omega}' G_1^T(\vec{\boldsymbol{r}}, \hat{\Omega}', \tau) g_1^s(\hat{\Omega}, \hat{\Omega}', \tau) f(\hat{\Omega}, \hat{\Omega}') + S(r, \hat{\Omega}). \tag{4}$$

In the CTE, $G_1^T(\vec{\boldsymbol{r}}, \hat{\Omega}, \tau)$ is the unnormalized temporal electric field correlation function, $f(\hat{\Omega}, \hat{\Omega}')$ is the probability of scattering from $\hat{\Omega}'$ into $\hat{\Omega}$. The variable μ_t is equal to the sum of the scattering and absorption coefficients, μ_s and μ_a. The angle θ is measured at the point of deflection from a scattering particle with respect to its initial angle of incidence and $S(\vec{\boldsymbol{r}}, \Omega)$ is the spatial distribution of the light source at position $\vec{\boldsymbol{r}}$**.**

While similar in form to the RTE, the CTE's additional term $g_1^s(\hat{\Omega}, \hat{\Omega}', \tau)$ accounts for the accumulation of decay of the correlation function resulting from each individual scattering event. This term $g_1^s(\hat{\Omega}, \hat{\Omega}', \tau)$ originates from the principles of dynamic light scattering (DLS) and is written as

$$g_1^s(\tau) = exp\left[-\frac{1}{6} 2k_0(1 - \cos\theta)\langle \Delta r^2(\tau)\rangle\right]. \tag{5}$$

Substituting in the expression for $g_1^s(\tau)$ as shown in Eq. (5) and applying the P_1 approximation, the CTE reduces to the correlation diffusion equation for a semi-infinite turbid medium [8]

$$\left(D_\gamma \nabla^2 - \mu_a - \frac{1}{3}\mu_s{}' k_0^2 \langle \Delta r^2(\tau)\rangle\right) G_1(\vec{\boldsymbol{r}}, \tau) = -S(\vec{\boldsymbol{r}}) \tag{6}$$

in which $S(\vec{\boldsymbol{r}})$ is the spatial distribution of the light source at position $\vec{\boldsymbol{r}}$ in space, μ_a is the absorption coefficient, and $\mu_s{}'$ is the reduced scattering coefficient [19, 21]. Terms k_0^2 and D_γ refer to the wavenumber and the photon diffusion coefficient $D_\gamma = \frac{1}{3(\mu_a + \mu_s')}$, respectively whereas $\langle \Delta r^2(\tau)\rangle$ represents the mean-square displacement of path lengths.

An analytical solution to the correlation diffusion equation similar to the photon diffusion equation is

$$G_1(\vec{\boldsymbol{r}}, \tau) = \frac{3\mu_s'}{4\pi}\left(\frac{\exp(-Kr_1)}{r_1} - \frac{\exp(-Kr_2)}{r_2}\right). \tag{7}$$

In the exponential, $K = 3\mu_a\mu_s{}' + \mu_s'^2 k_0^2 \langle \Delta r^2(\tau)\rangle$ while $r_1 = [z_0^2 + \rho^2]^{1/2}$ and $r_2 = [(z_0 + 2z_b)^2 + \rho^2]^{1/2}$ where ρ is the distance parallel to the sample boundary, z_0 is the random walk step equivalent to $1/\mu_s'$ and finally z_b is the extrapolated zero boundary equal to $\frac{2}{3\mu_s'}\frac{1+R_{eff}}{1-R_{eff}}$ where R_{eff} is the effective reflection coefficient of the medium [23].

In the analytical solution to the correlation diffusion equation, the mean square displacement of path lengths, $\langle \Delta r^2(\tau)\rangle$, is modeled using one of two expressions. The first of

which assumes the scattering particles are undergoing Brownian or diffusive motion and is written as $\langle \Delta r^2(\tau) \rangle = 6\alpha D_B \tau$ where D_B is the effective Brownian diffusion coefficient for particles within the medium ($D_B = \frac{kT}{6\pi\eta a}$ where k is the Boltzmann constant, T is the temperature, η is the viscosity of the medium, and a is the particle radius), α is a ratio of static to moving scatterers and lies between 0 and 1, and τ is the correlation time [8, 24-26]. The mean square displacement of path lengths, $\langle \Delta r^2(\tau) \rangle$, could also be satisfied by assuming the scattering particles are under directed flow, also known as the random flow model, $\langle \Delta r^2(\tau) \rangle = V^2\tau^2$ where V is the velocity of the scatterers and τ is the correlation time.

Although it is widely accepted that the Brownian flow model $\langle \Delta r^2(\tau) \rangle = 6\alpha D_B \tau$ fits DCS data more closely [27-29], the experiments discussed here suggest that fitting is dependent on the experimental conditions. While experimental details will be discussed in upcoming sections of this thesis, Figure 3 demonstrates how fitting resolution is a function of experimental parameters. Figure 3a depicts a DCS scan taken on a flow channel filled with scattering solution with an optical reduced scattering coefficient of 12 cm^{-1} and absorption coefficient of 0.075 cm^{-1}. While details of the shape of DCS autocorrelation curves will be discussed in future sections of this thesis, data shown depicts DCS measurements taken with a single mode fiber (1.5 mm source-detector separation) when there was a flow channel submerged 0 mm. In Figure 3a, the solution within the flow channel was not experiencing directed flow, with diffusive motion being the main contributor to the autocorrelation curve. It is evident that the Brownian flow model fit matches the experimental data much more closely than the random flow model fit when there is no directed flow in the channel. On the contrary, when there is directed flow within the flow channel, (flow 3 = 0.05 cm/s) as shown in Figure 3b, the random flow model $\langle \Delta r^2(\tau) \rangle = V^2\tau^2$ fits the data much more closely. The flowing and surrounding solution were made to have. The flowing solution had a velocity set to 0.05 cm/s within the flow channel.

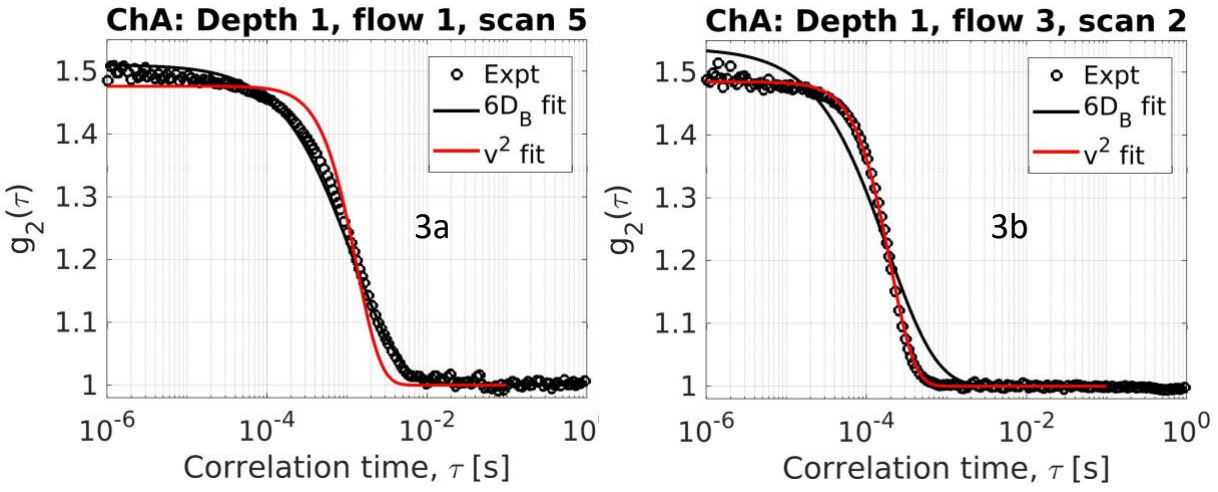

Figure 3: DCS experimental data (black circles) shown with the Brownian fit (block solid line) as well as the random fitting (red solid line) for the case of no flow (flow 1 = 0 cm/s) and flow (flow 3 = 0.05 cm/s). The Brownian fit matches the data more closely than the random fit.

2.2 Experimental Determination of the Normalized Intensity Autocorrelation Function

In conjugation with theoretical predictions of the unnormalized electric field autocorrelation function, $G_1(\vec{\boldsymbol{r}},\tau)$, one can experimentally determine this value for comparison. The normalized intensity field correlation function, $g_2(\vec{\boldsymbol{r}},\tau)$ can be calculated by monitoring temporal fluctuations in the incident intensity fields at the photodetector and calculated using a digital autocorrelator board. The normalized temporal intensity autocorrelation is related to the normalized and unnormalized temporal electric field autocorrelation functions, $g_1(\vec{\boldsymbol{r}},\tau)$ and $G_1(\vec{\boldsymbol{r}},\tau)$, respectively through the Siegert relation, $1+\beta|g_1(\vec{\boldsymbol{r}},\tau)|^2 = g_2(\vec{\boldsymbol{r}},\tau)$ which is based on the relationship $I(\vec{\boldsymbol{r}},t) = E(\vec{\boldsymbol{r}},t)E^*(\vec{\boldsymbol{r}},t) = |E(\vec{\boldsymbol{r}},t)|^2$. These relations are

$$g_1(\vec{\boldsymbol{r}},\tau) = \frac{\langle \vec{E}(t)\cdot\vec{E}^*(t+\tau)\rangle}{\langle \vec{E}(t)\cdot\vec{E}^*(t)\rangle} \tag{8}$$

and

$$\frac{1+\beta|G_1(\vec{\boldsymbol{r}},\tau)|^2}{\langle I(\vec{\boldsymbol{r}},0)\rangle^2} = 1+\beta|g_1(\vec{\boldsymbol{r}},\tau)|^2 = g_2(\vec{\boldsymbol{r}},\tau) = \frac{\langle I(\vec{\boldsymbol{r}},0)\cdot I(\vec{\boldsymbol{r}},\tau)\rangle}{\langle I(\vec{\boldsymbol{r}},0)\rangle^2}. \tag{9}$$

In the Siegert relation, β is inversely proportional to number of speckles recorded at the detector, $\vec{\boldsymbol{r}}$ the position vector, τ is the correlation time, I is the intensity, $\vec{E}(t)$ is the electric field as a function of time along with its complex conjugate denoted by the asterisk, and angular brackets represent an ensemble average, meaning it is unique to a given microstate that the system is in at that instance [13, 24, 30].

In general, diffusion theory is valid if two assumptions are made: 1) the number of scattering particles is much greater than the number of absorbing particles within the medium and 2) photons have undergone multiple scattering events before reaching the detector. These conditions are typically met by choosing a source with sufficiently low absorption in the medium of interest and by ensuring that the source-detector separation of the fiber geometry is significantly larger than the average path length of the photons [8, 25].

2.3 Instrumentation

2.3.1 The Light Source

DCS employs a coherent (coherence length of usually a couple meters) light source that operates in the near-infrared (NIR) region of the electromagnetic spectrum, usually between 750-800 nm. DCS is implemented to analyze relative changes in flow in biological samples, such as tissues, making NIR wavelengths desirable due to their low absorption. A laser is chosen as the light source in DCS due to the inherent nature of its speckle pattern that it produces. This speckle pattern results from the interfering light waves from the laser; the bright spots being a result of

constructive interference and the dark spots, destructive interference. Figure 4 below depicts an example of this characteristic speckle pattern that appears on a black cloth screen from an incident helium-neon laser source operating at 633 nm. Perturbations to this speckle pattern can be studied to gain insight to various optical properties of the sample.

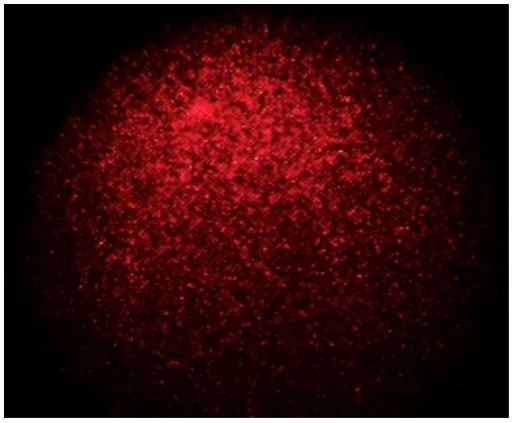

Figure 4: An example of a laser speckle pattern that resulted from a He-Ne laser.

Figure 5 depicts the autocorrelation curves that resulted from DCS scans collected on a solid phantom block with scattering properties using both a 785-nm coherent (coherence length <10m) laser as well as an incoherent helium-neon light source.

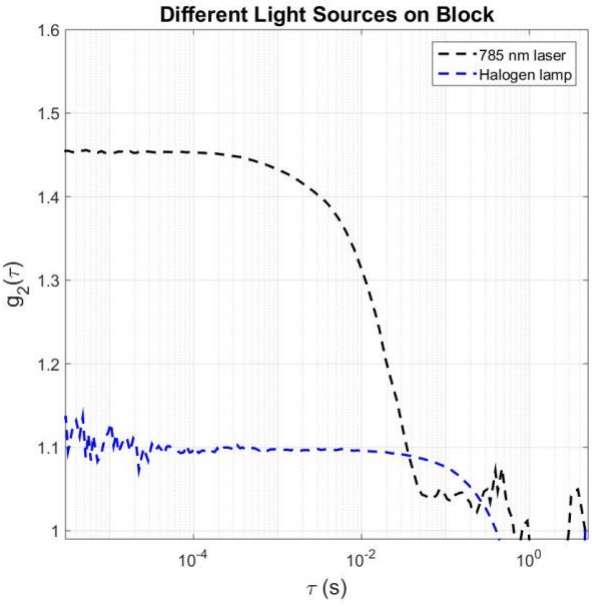

Figure 5: DCS scans on a phantom block from both a coherent 785 nm laser (black dotted line) and a non-coherent Halogen lamp (blue dotted line).

As shown in Figure 5, there are clear distinctions between the DCS data taken with the coherent (785 nm) versus the incoherent (halogen lamp) sources. As represented through the blue dotted line in Figure 5, an incoherent source such as the halogen lamp produces a signal that lacks

decorrelation due to its inability to retain its interference properties as the light diffuses through the turbid sample. A coherent source, such as the 785-nm laser with a coherence length greater than 10 meters will provide a characteristic decorrelation curve as a result of Brownian motion or directed flow within the sample being probed as previously discussed.

2.3.2 Fiber Optic Probes

DCS uses a single mode fiber optic probe to detect the backscattered laser light from the sample in order to monitor the temporal intensity fluctuation of one (to a few) speckles. A single mode fiber is optimal for DCS because only one to a few speckles need be detected in order to gain information about perturbations to the sample one is probing and ensure an adequate signal-to-noise ratio for the data. One distinguishing factor between multimode and single mode fibers is the amount of light modes that they are able to support within the fiber. A single mode fiber is restricted to a single light mode, while a multimode fiber can support multiple modes of light, often leading to low signal-to-noise ratio in DCS.

DCS measurements collected on an index finger with a 785 nm long coherence length (>10 m) laser source using both a single mode (5 μm diameter) and a multimode (400 μm diameter) detection fibers are shown below in Figure 6.

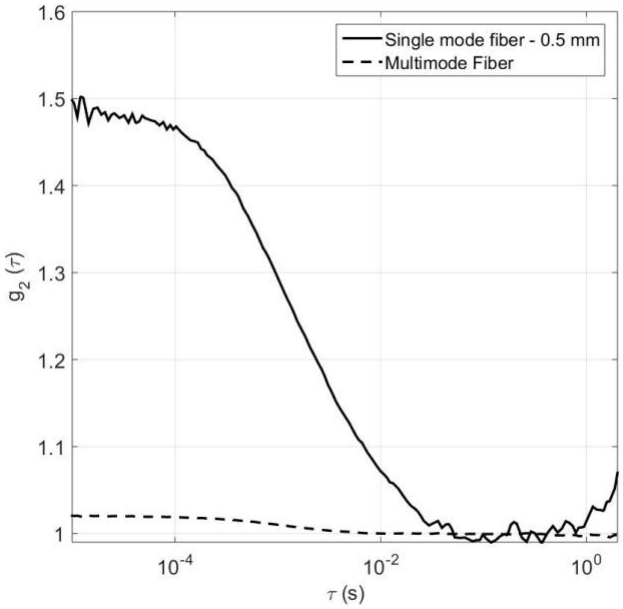

Figure 6: DCS scans taken on index finger using a single mode fiber with a source-detector separation of 0.5 mm (shown as the solid line) and also with a 400-micron multimode fiber (shown as the dotted line).

The solid black line represents a DCS scan taken on an index finger with a single mode (5 micrometer) detector fiber. With a single mode detection fiber, the temporal fluctuations in backscattered light intensity from one to a few speckles can be monitored to achieve a sufficient signal-to-noise ratio. This results in the characteristic decay of the autocorrelation curve. On the other hand, if a multimode detection fiber is utilized in the DCS setup, it will result in a low sign-to-noise ratio as a result of multiple speckles being in the detection field. As shown by the dotted

black line in Figure 6, when a multimode detection fiber is implemented, there is no characteristic decay of the DCS autocorrelation curve.

In addition to the size of the detection fiber, the distance between the source fiber, which delivers the light, and the detection fiber also plays an important role in DCS. The source-detector separation (often notated as ρ) determines the depth at which the DCS system can sense into the sample. Typically, it is accepted that the probing depth is approximately one half of the source-detector separation [13].

2.3.4 Photon Counting and Processing Systems

The photons detected through the single mode detection fiber are relayed to an avalanche photodiode (APD) set in the Geiger mode. In the Geiger mode, the APD operates on the probability of whether a photon will result in a detection signal. For example, if the avalanche of electrons initiated by the photon within the APD is short-lived, no signal will be produced. On the other hand, if the avalanche effect is sufficient, the APD will transduce light into voltage by exploiting the photoelectric effect to initiate a cascade of signal amplification within a semiconducting device. The resulting signal from the APD is a plot of intensity versus time which can then be sent to an autocorrelator board. The autocorrelator produces the characteristic autocorrelation function for DCS. An overview of the general DCS experimental setup is shown below in Figure 7.

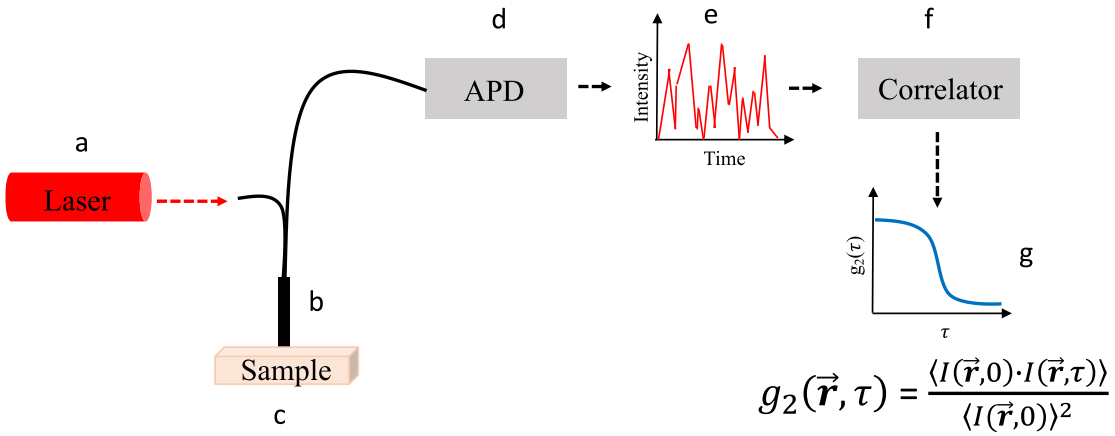

Figure 7: DCS Setup. Components are as follows: a) coherent, near infrared laser source, b) single mode fiber probe, c) sample comprised of scattering and/or absorbing particles, d) Avalanche photodiode (APD), e) intensity vs time plot, f) autocorrelator board, g) measured $g_2(\vec{r},\tau)$ function.

The normalized intensity autocorrelation function, $g_2(\vec{r},\tau)$, produced by the correlator board provides a characteristic decay rate, which is related to the relative flow rates of the scattering particles [8]. Therefore, changes in this curve can be an indicator of various changes to flow rates. When DCS is used to measure a system in which the scattering particles are moving with high flow rates, the autocorrelation curve decays much faster compared to when the scattering particles have low flow rates. An example of this variation in decay rates is shown below in Figure 8.

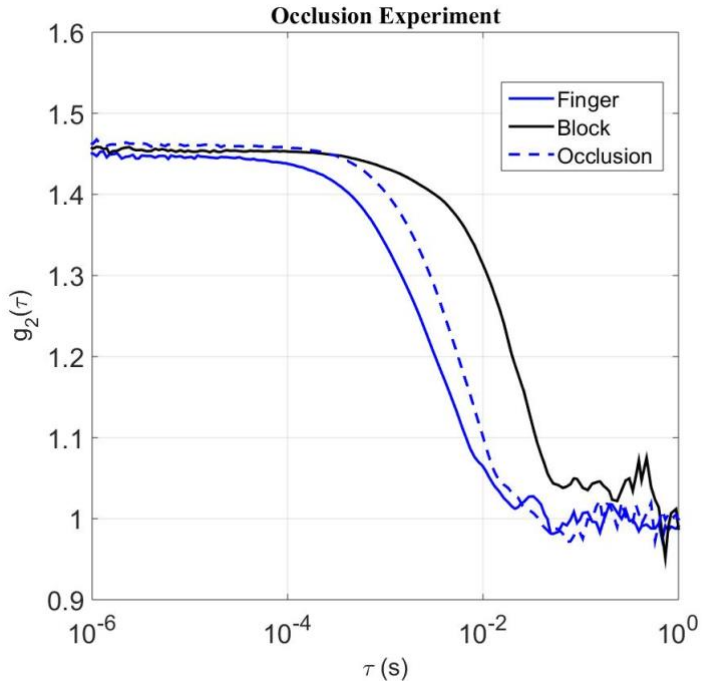

Figure 8: Occlusion experiment with a 200-micron single mode fiber probe.

This figure represents data taken on an index finger with a single mode (200 μm source and 5 μm detector) fiber optic probe. The black solid line represents a measurement taken on a phantom block where no directed flow is present. The solid blue line represents a measurement taken on an index finger while the arm was at rest on a table. As expected, the autocorrelation curve shifts to the left with a faster decay rate as a result of the directed blood flow naturally present in the probing volume of the finger. The blue dashed line represents a DCS measurement taken ten seconds after the index finger was occluded with a rubber band. When the rubber band is wrapped tightly around the index finger, it partially occludes the vessels, decreasing blood flow in the probed volume and therefore resulting in a slower decay of the autocorrelation curve.

2.4 Implementing DCS as a Tool for Monitoring Relative Changes in Blood Flow Rates

DCS has been implemented in in a variety of clinical settings to evaluate and optimize its flow-sensing capabilities [4, 9, 11, 12, 17, 31-35]. Having the capability to continuously determine changes in blood flow is critical to successfully monitoring many diseases that affect hemodynamic equilibrium in comparison to a healthy patient. Examples of these afflictions include but are not limited to the monitoring of cancer therapy treatments, monitoring of cerebral blood flow, possible early detection of ischemic strokes, and other medical conditions such as hypo and hypertension in which blood flow rates deviate from the norm. Frequent monitoring of these ailments not only allows for more accurate progression and treatment but also for medical professions to develop a treatment plan on a patient-by-patient basis rather than generalizing the disease and developing a prognosis based on that generalization [4, 13, 36, 37]. However, for this to be plausible there must be a form of non-invasive and readily accessible flow-monitoring

system that can be offered patients at an affordable cost. Current therapy monitoring techniques include computed tomography (CT), functional magnetic resonance imaging (fMRI), and positron emission tomography (PET) scans. Though effective, their high cost and immobility in addition to the possibility of exposure to harmful radiation in some imaging techniques limits the frequency at which the patient can undergo such imaging. While alternative flow-sensing techniques such as laser speckle contrast imaging (LSCI) [38, 39], Doppler optical coherence tomography (DOCT) [40, 41], and laser Doppler flowmetry (LDF) exist, they cease to provide patients with a non-invasive and affordable imaging technique that has the capability to sense beyond a few hundred microns beneath the surface. Near-infrared diffuse correlation spectroscopy (NIR-DCS) is capable of sensing relative blood flow changes up to a few centimeters within the human body making DCS an affordable, convenient, and efficient way to monitor those in need of bedside or frequent testing. DCS has been validated as a non-invasive method of measuring relative flow rates in many clinical diagnostic and monitoring applications such as detection of cancer, early indicators or ischemic stroke symptoms, and burn and would healing [4, 35, 42-44]. DCS serves as a promising alternative to these more traditional imagining devices such as functional magnetic resonance imaging (fMRI) and computed tomography (CT).

CHAPTER 3: THE EFFECT OF OPTICAL PROPERTIES ON DCS MEASUREMENTS

In DCS, the acquired measurements are connected to the rate of decay of intensity correlations, which in turn are dependent on all temporally changing quantities in the medium. In biological tissues, the scattered field from the motion of red blood cells within vasculature is considered the main contributing factor to the decay of the intensity correlations. However, since the detected multiply scattered photons can be expected to have interacted with both the background ("static") scatterers as well as moving ("dynamic") scatterers, several reports have studied the influence the optical properties of the medium have had on derived blood flow indices in DCS [45, 46]. The purpose of these experiments was to determine how altering the optical properties of the medium surrounding a submerged flow channel affect DCS's sensitivity to distinguishing between flow rates.

It has been reported that the sensitivity of DCS to monitor changes in buried flow is decreased by existing uncertainties in the absorption and scattering properties of the medium suggesting these optical properties contribute to the correlation function [25, 26]. Reports have shown error due to influences of optical properties surrounding a flow channel can be reduced by utilizing multi-distance diffuse correlation spectroscopy in conjugation with near-infrared diffuse optical spectroscopy to simultaneously sense buried flow within a turbid medium in addition to more accurately extract the optical properties of the sample [47].

The experiments discussed in this thesis examine the sensitivity of DCS in detecting directed flow of a scattering fluid within a channel embedded in a turbid medium. These experiments investigated the impact of varying flow speeds when the channel is embedded at increasing depths from the surface of the surrounding medium while also investigating how the flow sensitivity was impacted when the optical properties of the surrounding media were varied (for fixed properties of the flowing media).

3.1 Investigation of Flow Channel Depth and Various Optical Properties on DCS Measurements

3.1.1 Experimental Setup

A transparent plastic flow chamber 6.5 cm wide by 6.5 cm long by 1.0 cm tall was created in which 1.6 mm inner diameter (3.2 mm outer diameter) plastic PVC tubing was attached to the bottom of the chamber using Sugru™ putty as shown in Figure 10.

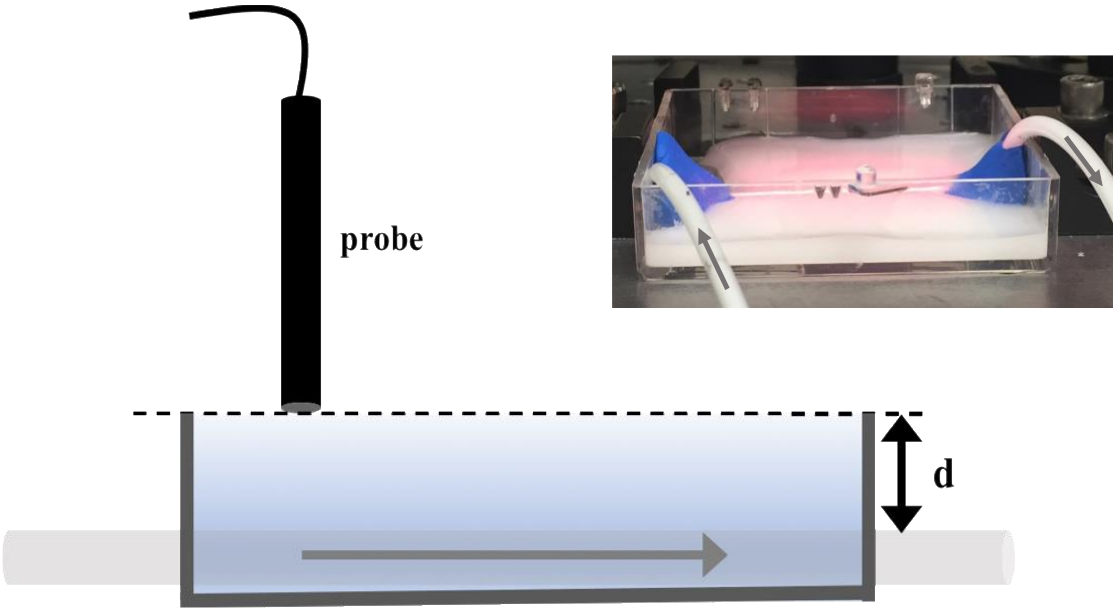

Figure 9: Experimental flow chamber.

In the experiments reported here, the flowing solution consisted of 1.0 μm diameter polystyrene microspheres (Polybead microspheres, 07310, Polysciences Inc., Warrington, PA) suspended in deionized (DI) water with μ_s' of 24 cm^{-1} at 785 nm as calculated using Mie theory [48, 49]. The absorption coefficient of the flowing solution was considered negligible.

Two separate experiments were conducted. In the first, the depth of the flow channel from the top surface was varied by addition of fluid to the container. Having known the volume of the container, the amount of solution needed to increase the depth of the flow channel by a certain amount could be precisely calculated. In these experiments, the depth was increased by 0.3 mm. The "0 mm" point was taken where there was just enough solution in the chamber to cover the flow channel. DCS measurements were obtained from each phantom the as the fluid was pumped through the channel using a syringe pump for flow rates of 0 mL/min (pump turned off), 3 mL/min and 6 mL/min. Three repeat DCS scans were taken at each measurement point.

In the second study, the depth of the flow channel was kept fixed at 0.6 mm while the surrounding medium's optical properties were varied. DCS measurements were obtained from each phantom the as the fluid was pumped through the channel using a syringe pump for flow rates of 0 mL/min (pump turned off), 3 mL/min and 6 mL/min with three repeat DCS scans. Data for both the depth study and the study to determine the effect of optical properties on the flow chamber were collected for fiber source-detector separations of both 1.5 mm (ChA) and 0.5 mm (ChB). Table 1 below shows the nomenclature that will be utilized through the experiments presented in this thesis.

Table 1: Description of symbols used in the experiments.

Symbol	Description
d	Describes the depth of the flow channel with respect to the surface of the phantom solution.
f	Describes the flow rate/velocity through the flow channel as set on the software controlling the syringe pump.
ChA	Refers to a source-detector separation of 1.5 mm on the DCS probe.
ChB	Refers to a source-detector separation of 0.5 mm on the DCS probe.

3.1.2 Increasing the Depth of the Flow Channel

The first set of experiments was conducted to observe changes in the sensitivity of DCS measurements for detecting flow in a buried channel, as the depth of the channel (d in Figure 10) from the surface was increased. As discussed above, the solution in the flow channel had a μ_s' of 24 cm^{-1}. During sample preparation, enough of this was prepared to consider this a stock solution. From the stock, a 1:4 dilution was conducted to achieve a μ_s' of 6 cm^{-1} at 785 nm. The surrounding medium was taken to have negligible absorption.

In these studies, the depth of the channel was varied by adding constant volumes of the surrounding fluid to the container thereby raising the fluid surface in the container. The depth of the channel from the surface was varied from 0 mm and increased in steps of 0.3 mm until 2.7 mm – these ten phantoms are referred to as D1 (d=0 mm) through D10 (d=2.7 mm). For the start of the experiment, the container was filled until the surrounding medium just submerged the flow tube where the depth was set to 0 mm. By knowing the volume of the flow chamber, it was determined that 1.4 mL of solution equated to a depth increase of 0.3 mm. Throughout the experiment, the fluid surface was raised appropriately by 300 μm after each set of DCS measurements.

3.2.3 Varying Optical Properties of Surrounding Media

The second study investigated the observed changes in DCS measurements when acquired from the flow channel kept at a fixed depth of 600 μm from the surface while the optical properties of the surrounding were changed. Table 2 provides the optical properties of the surrounding media tested in this study.

Table 2: Optical properties of surrounding medium.

Phantom ID	Absorption Coefficient (cm^{-1})	Reduced Scattering Coefficient (cm^{-1})
P1	0.02	3.0
P2	0.08	3.0
P3	0.02	6.0
P4	0.08	6.0

Each liquid phantom was prepared mixing a given V_1 volume of 1 μm diameter polystyrene spheres to V_2 volume absorber and finally adding V_3 volume of DI water (to achieve a total phantom volume of 17.6 mL such that the flow channel lay nearly 600 μm beneath the liquid surface). Absorber solutions were prepared by dissolving bovine hemoglobin (H3760; MilliporeSigma, MO) in DI water and calculating its absorption coefficient using a spectrophotometer (Cary 100 UV-Vis, Agilent Technologies, Wilmington, DE). Final absorption and scattering properties were calculated using the spectrophotometer measurements and Mie theory, respectively, and were selected to represent values reported for the human forearm [50].

The DCS data was obtained first by positioning the fiber probe on each phantom such that the tip was judged to make first contact with surface as it was moved directly perpendicular toward it, from above. The probe was centered relative to the edges of the phantom container and oriented such that the line through the center of the source and detector fibers lay nearly perpendicular to that of the flow channel. Three repeated scans were recorded for each flow rate tested in every phantom. Numerical code written in MATLAB® (Mathworks, Natick, MA) was used to process the acquired DCS measurements.

3.2.4 Experimental Data & Results

3.2.4.1 Data Analysis

The measured DCS data was fit using the theoretical diffusion model of particle motion where the unnormalized electric field autocorrelation function is

$$G_1(\vec{\boldsymbol{r}},\tau) = \frac{3\mu_s'}{4\pi}\left(\frac{\exp(-Kr_1)}{r_1} - \frac{\exp(-Kr_2)}{r_2}\right). \tag{10}$$

as described in Section 2.1. The data was fit utilizing two free parameters, αD_B and β (which was the intercept of $g_2(\tau)$ at $\tau = 0$) [28]. Figure 10a shows DCS measurements (circles) and fits (lines) using the Brownian flow DCS model for data obtained at two flow speeds when the flow channel was not submerged.

It was found that the Brownian flow model fits used did not match well with the experimental data, especially in cases when there was directed flow within the flow channel. As seen in Figure 10a when the flow pump was set to 6 mL/min, a double exponential appeared in the decay of the autocorrelation function [51]. In order to more closely match the experimental data, an empirically constructed, two-component exponential

$$g_2(\tau) = 1 + \alpha_1 e^{\frac{-\tau}{\tau_1}} + \alpha_2 e^{\frac{-\tau}{\tau_2}} \tag{11}$$

was implemented. Figure 10b shows these same measurements but when fit using the two-component exponential model. The data in Figure 10 represents DCS measurements collected with a source-detector separation of 1.5 mm (ChA).

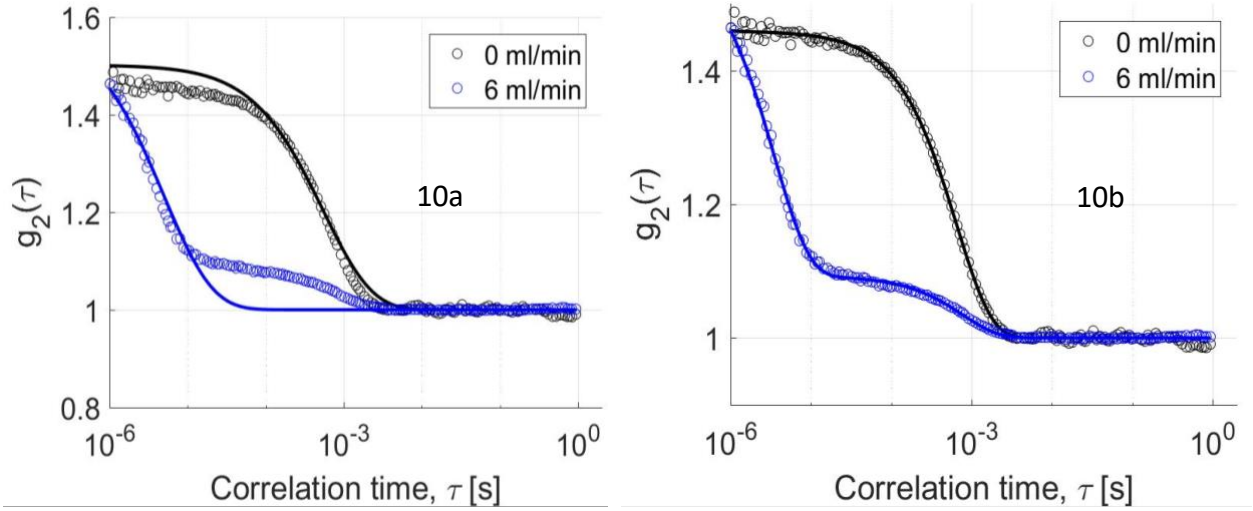

Figure 10: Measured DCS scans for the depth-phantom D1 (flow channel at d = 0 mm) at two flow speeds (black symbols for 0 mL/min and blue for 6 mL/min). Lines show the fits to measured data calculated using the Brownian flow DCS model (10a) and Eq. (11) (10b).

As seen in Figure 10, the two-component exponential model in Eq. (11) has better residuals in fitting data relative to the DCS Brownian flow model. For the two-component model, τ_1 was constrained to lie between 1 μs and 1ms, while τ_2 was constrained to be between 0.1 ms and 1 s. Parameters α_1 and α_2 were constrained to lie between 0 and 1. It is worth noting that, the sum of α_1 and α_2 from the two-exponential fits would be β from the Siegert relation.

3.2.4.2 Results for Varying the Depth of the Flow Channel Submersion

In order to determine the effect that increasing the depth of the flow channel had on DCS sensitivity, each of the three repeated DCS acquisitions were parameterized using either the diffusion theory-based Brownian flow model to obtain a value of αD_B or the two-component

model (Eq. (11)) to obtain A_1 [52]. The sensitivity to flow parametrized using Eq. (11) was made using A_1, calculated as

$$A_1 = \frac{\alpha_1\tau_1}{\alpha_1\tau_1+\alpha_2\tau_2} \quad . \tag{12}$$

The three repeat DCS scans were then combined using the mean and standard deviations, of each derived parameter, for each phantom and flow-speed. Figure 11 depicts the DCS fit parameters for the diffusion theory-based (Figure 11a and 11b) and double exponential fits (Figure 11c and 11d) for both source-detector separations.

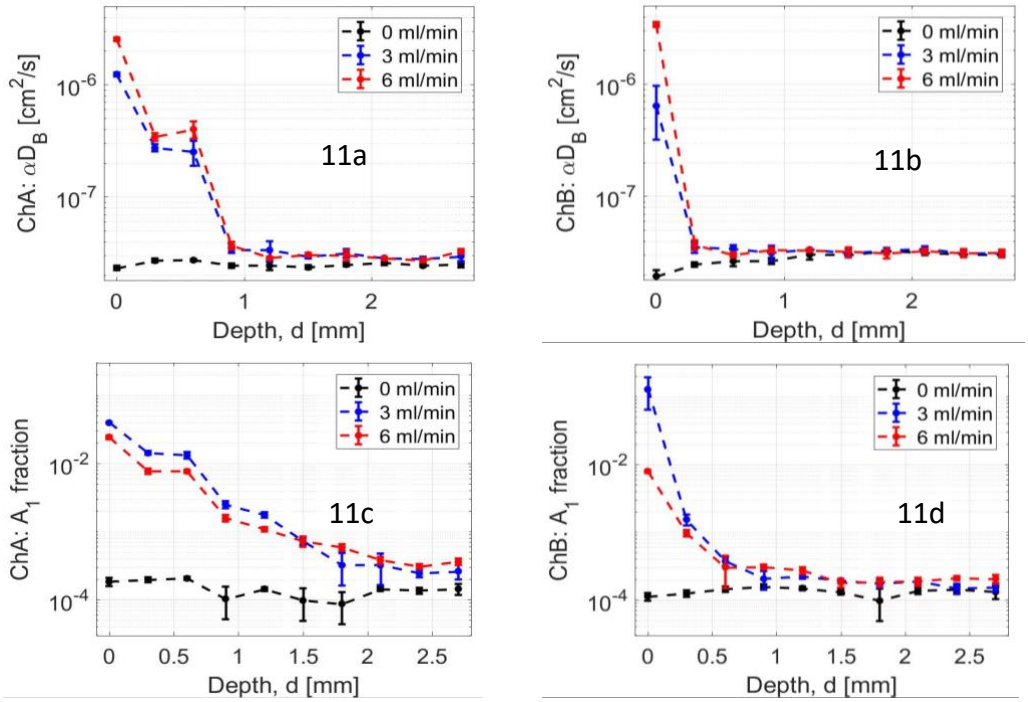

Figure 11: DCS measured flow rates for all depth-varying phantoms across the three pump speeds for both ChA (1.5 mm source-detector separation) and ChB (0.5mm source-detector separation). Data in 11a and 11b shows the diffusion theory derived fit-parameters, while 11c and 11d show the A_1 fraction using Eq. (11). Symbols are mean values and error bars standard deviation.

For both fits the computed flow index, either αD_B for the Brownian flow model or the A_1 parameter derived from the two-component exponential model, decreased as the volume of scattering medium burying the flow channel was increased. The diffusion theory-based Brownian flow model parameter, αD_B, retained sensitivity to distinguish between three flow speeds up to a depth of 600 μm for a source-detector separation of 1.5 mm (ChA). For a source-detector separation of 0.5 mm (ChB), sensitivity diminished between the three flow speeds as the flow channel submersion becomes 300 μm depth.

Similarly, the parameter, A_1 (derived from the two-component model Eq. (11)) retained sensitivity to three flow speeds up to a depth of 1200 μm for ChA and 300 μm for ChB. While distinguishability between flow speeds is retained until a depth of 1200 μm for ChA, Figure 11 suggests that the A_1 parameter is more sensitive to relatively moderate flow speeds as opposed to higher ones, as the data for 3 mL/min is shown to have higher flow parameters than that for 6 mL/min for both ChA and ChB.

Both DCS flow indices, αD_B for the Brownian flow model or the A_1 parameter derived from the two-component exponential model, for each phantom were normalized to their matching index for a flow rate of 0 mL/min when the tube was not submerged (D1). This normalization allowed for a further analysis of the effects that the buried depth on the DCS measurements and scaled the data to be able to make better comparisons between the experimental or analytical approaches. The decrease in distinguishability between the flow rates shown for both systems is seen in Figure 12. Blue symbols represent DCS data fit using the two-component exponential model as described in Eq. (11) while red symbols represent DCS data fit using the Brownian flow model. Circles, triangles, and squares represent the mean of three repeat DCS scans taken at 0, 3, and 6 mL/min respectively for both the two-component exponential and Brownian flow model fits. Error bars indicate the standard deviation across the three repeat DCS scans.

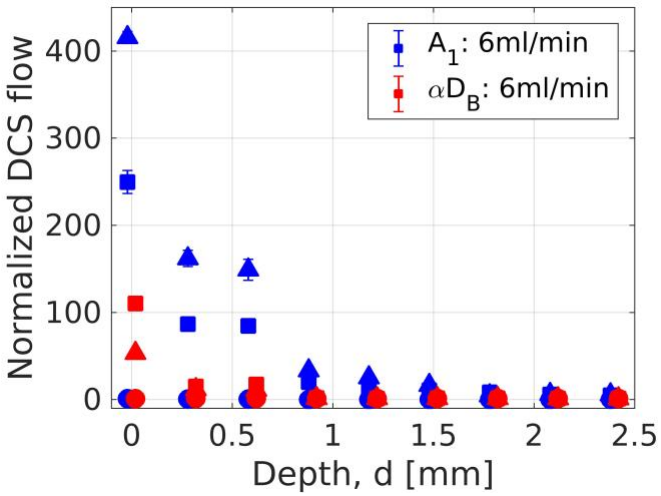

Figure 12: ChA DCS data that was normalized to the A1 (blue) or αDB (red) for D1, zero flow. Triangles represent 6 mL/min, squares represent 3 mL/min, and circles represent 0 mL/min.

Data presented here suggests that the DCS system's sensitivity to varying flow rates decreased with increasing flow channel submersion. For ChA, at d = 0 μm, the normalized DCS A_1 fraction for the 3 mL/min and 6 mL/min was 415 ± 82.6 and 249 ± 47.2, respectively. This data suggests that the A_1 fraction may be hypersensitive to lower flow speeds due to the normalized DCS flow values for 3 mL/min being greater than that for 6 mL/min. The normalized αD_B values at d = 0 μm for 3 mL/min and 6 mL/min were 53.2 ± 0.47 and 110 ± 3.2. At a flow

channel submersion depth of D4 (d = 900 μm), normalized flow indices decreased to 33.3 ± 6.3 and 20.0 ± 4.2 for the A_1 fraction and 1.45 ± 0.07 and 1.58±0.05 for αD_B. Beyond this analysis, ChB was not considered due to its rapid loss of sensitivity between flow rates sensitivity with the first addition of solution to the flow chamber. Detailed analysis was reserved for ChA, which had the larger source-detector separation of 1.5 mm.

3.2.4.3 Results for Varying Optical Coefficients of the Surrounding Medium

Following the depth-controlled experiment, the effect of varying the optical properties of the medium surrounding the flow channel on DCS sensitivity was examined. For this study, the depth of the flow channel was held constant at 600 μm while only the optical properties of the solution surrounding the buried channel were varied. The optical properties of the surrounding solution for this study are shown in Table 2.

DCS measurements were analyzed using both the Brownian flow model to achieve a flow indices, αD_B, and the A_1 parameter derived from the two-component exponential model. Identical to the depth-controlled study, all DCS data was. All DCS measurements were normalized to the no submersion (D1), zero flow measurement. Figure 13 shows the results of this analysis. Bars represent mean values across the three repeated data acquisitions while error bars denote standard deviations across these three repeat DCS measurements.

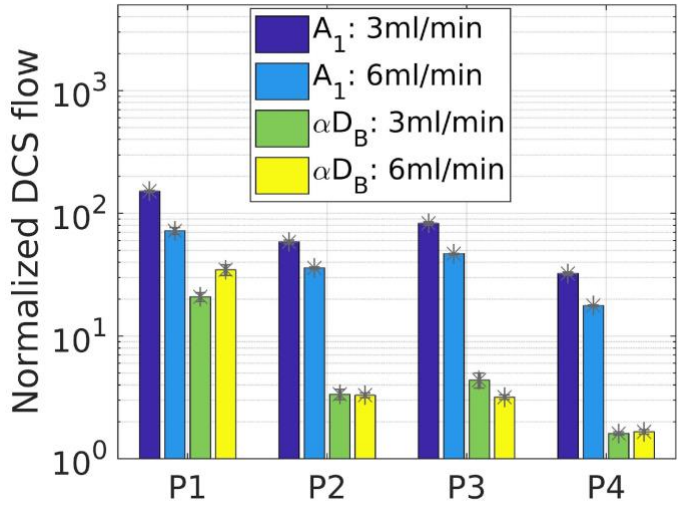

Figure 13: ChA DCS flow data that was normalized to the appropriate A_1 or αD_B, value for the D1, zero flow case. Error bars are representative of standard deviation.

It can be seen from Figure 13 that the A_1 fraction had higher sensitivity to changes in flow than the αD_B parameter from the diffusion theory-based flow model. The A_1 fraction had increased sensitivity to moderate flow (i.e. 3 mL/min) in comparison to the higher flow rate as seen in phantoms P1-P4. The diffusion theory-based flow parameter, αD_B, also shows this behavior in P3 where the flow parameter is larger for the 3 mL/min flow rate in comparison to

the 6 mL/min flow rate. Additionally, Figure 13 suggests that absorption has a deteriorating effect on DCS sensitivity to flow. The low absorbing phantom, P3, even with high scattering has increased sensitivity of its flow indices.

3.2.5 Discussion of the Depth-Controlled and Variation of Optical Properties Studies

This study allowed for the conclusion that the DCS system's ability to sense between flow rates is affected by two things: 1) the depth of the flow channel and 2) the optical properties of the medium surrounding the flow channel. Although decreased sensitivity was shown to depend on depth of and optical properties surrounding a flow channel, questions remained regarding the significance of the data and how it could provide meaning to the biomedical community.

In order to be able to draw more direct and concise conclusions regarding the affect these variables had on DCS sensitivity, experimental modifications were made. First, it was determined that the large discrepancy between the reduced scattering coefficients of the flowing solution (24 cm^{-1}) and the surrounding solution (6 cm^{-1}) contributed to the ability of the DCS system to sense to depths up to 1200 μm. While *in vivo* the scattering coefficient of blood is higher than that of most tissues, it is unlikely the it is ≥ 4 times as much. In subsequent experiments, appropriate modifications were made so that the optical properties of both the surrounding and flowing medium were equivalent. This will eliminate the possibility in extenuating factors when assessing the ability of DCS to distinguish between flow speeds with an increase in flow channel submersion depth.

Considering how DCS has potential as a clinical model to monitor relative flow rates in microvasculature, the three flow rates utilized in these studies were examined. The flow rates utilized here were chosen to match a blood vessel of comparable size to *in* vivo. It was found that with DCS's depth sensing ability limited to microvasculature, it would be more appropriate to choose flow rates that are on the order of capillary flow. In the subsequent study, flow velocities were chosen to be 0, 0.02, 0.05, and 0.08 cm/s.

CHAPTER 4: THE EFFECT OF FLOW CHANNEL SUBMERSION DEPTH OF DCS MEASUREMENTS

4.1 Experimental Design of the Depth Study

The next task was to observe changes in sensitivity of DCS measurements to detecting flow in a buried channel, as the depth of the channel (d in Figure 9) from the surface was increased. The same flow chamber apparatus and experimental setup from the previous experiment was utilized. In this experiment, the flowing and surrounding solutions were prepared using detailed protocols to achieve target absorption and scattering properties so that the surrounding solution and the flowing solution were identical with regard to their optical properties. The liquid phantom consisted of 1.0 μm diameter polystyrene microspheres (Polybead microspheres, 07310, Polysciences Inc., Warrington, PA) suspended in deionized (DI) water with μ_s' of 12 cm^{-1} at 785 nm as calculated using Mie theory [53]. The liquid phantom also contained absorber, prepared by dissolving bovine hemoglobin (H3760; MilliporeSigma, MO) in DI water and calculating its absorption coefficient using a spectrophotometer (Cary 100 UV-Vis, Agilent Technologies, Wilmington, DE), to achieve a final absorption coefficient of μ_a of 0.075 cm^{-1}.

The depth of the flow channel was increased by adding constant volumes of the surrounding fluid to the container thereby raising the fluid surface in the container. This experiment utilized only a single source-detector separation, 1.5 mm. The depth of the channel from the surface was varied from 0 mm at the beginning and increased in steps of 0.3 mm to a maximum of 0.9 mm – referred to as D1 (d=0 mm) through D4 (d=0.9 mm). For the start of the experiment, the container was filled until the surrounding medium just submerged the flow tube (for the D1 phantom). DCS measurements were obtained at each depth as fluid was pumped through the channel using a syringe pump. The pump was set to one of four flow velocities: 0 cm/s (pump turned off), 0.02 cm/s, 0.05 cm/s, and 0.08 cm/s. Flow speeds were chosen to match much smaller vessels in vivo, such as capillary flow [51]. Five repeat DCS scans were taken for each set of measurements.

4.2 Data Analysis & Results

Experimental DCS data was fit with the Brownian flow model in which the derived flow parameter, αD_B, was examined. As seen in Figure 14, as the flow speed of the solution within the flow channel was increased to 0.08 cm/s, the αD_B parameter consequently increased. Data shown in Figure 14 represents the mean computed across the five repeat DCS measurements and is shown for four flow speeds (dashed lines) and each depth (circles). Standard deviations over these five repeat scans for each set of measurements is shown as error bars.

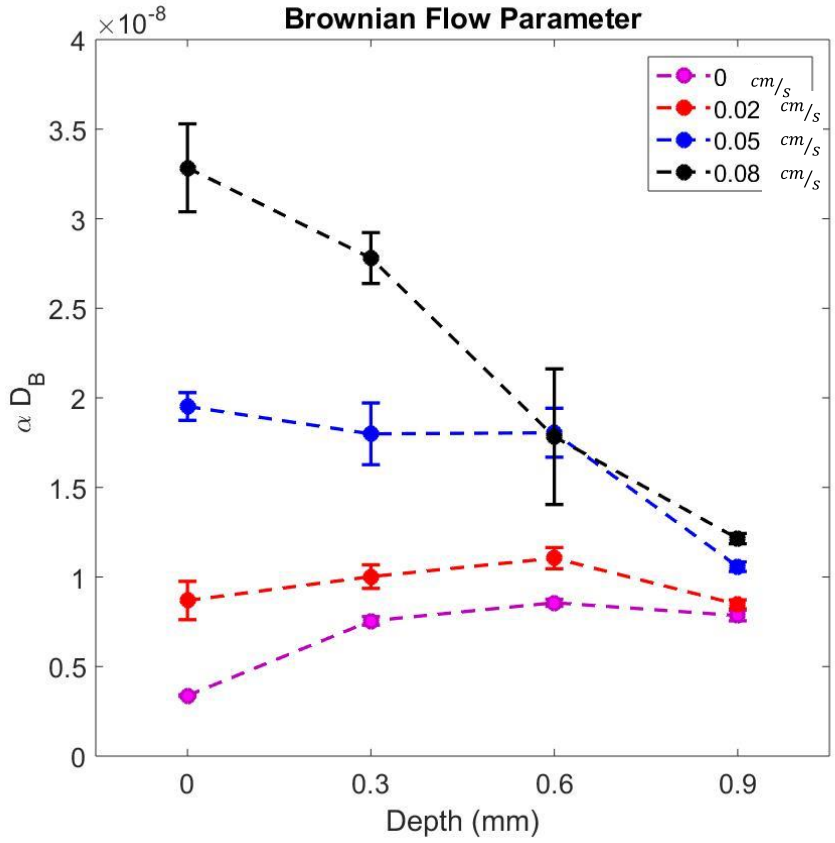

Figure 14: Depicts DCS Brownian flow parameter for all four depths (circles) and all four flow speeds (dashed lines).

As depicted in Figure 14 for the higher flow speeds, 0.05 and 0.08 cm/s, the αD_B parameter decreased with increasing submersion depth of the flow channel. Alternatively, for the lower flow speeds of 0 and 0.02 cm/s, this was not the case. Instead, the αD_B parameter for those lower flow speeds increased with increasing submersion depth of the flow channel. Recall that the αD_B parameter is a measure of relative flow rates being detected by the DCS system. Therefore, two predictions were made prior to this experiment: 1) as the flow speed is decreased, the αD_B parameter should also decrease and 2) as the depth of the flow channel is increased, the αD_B parameter should also decrease as a result of decreased DCS to sense buried flow. While for data taken at the higher flow speeds, the predictions are validated experimentally, the lower flow speeds do not match predictions. It is hypothesized that this is due to diffusive motion that is occurring above the flow channel when it is submerged. As the depth of the flow channel was increased, the amount of scattering and absorbing solution placed on top of the flow channel was also increased. Since this solution is optically dense, it is expected that it would experience some diffusive motion within, contributing to the increase in αD_B parameter that occurred.

In addition to the absolute αD_B parameter, the change in this parameter (ΔRBF) was also investigated. At each depth and for each flow speed, the change in the relative flow parameter, αD_B, was calculated. For example, the change in relative flow computed using the αD_B parameter from 0 to 0.08 cm/s was computed as $\Delta RBF = \alpha D_{B,0.08} - \alpha D_{B,0}$. Figure 15 depicts

ΔRBF plotted as a function of the absolute flow speeds in which the syringe pump was programmed to operate at.

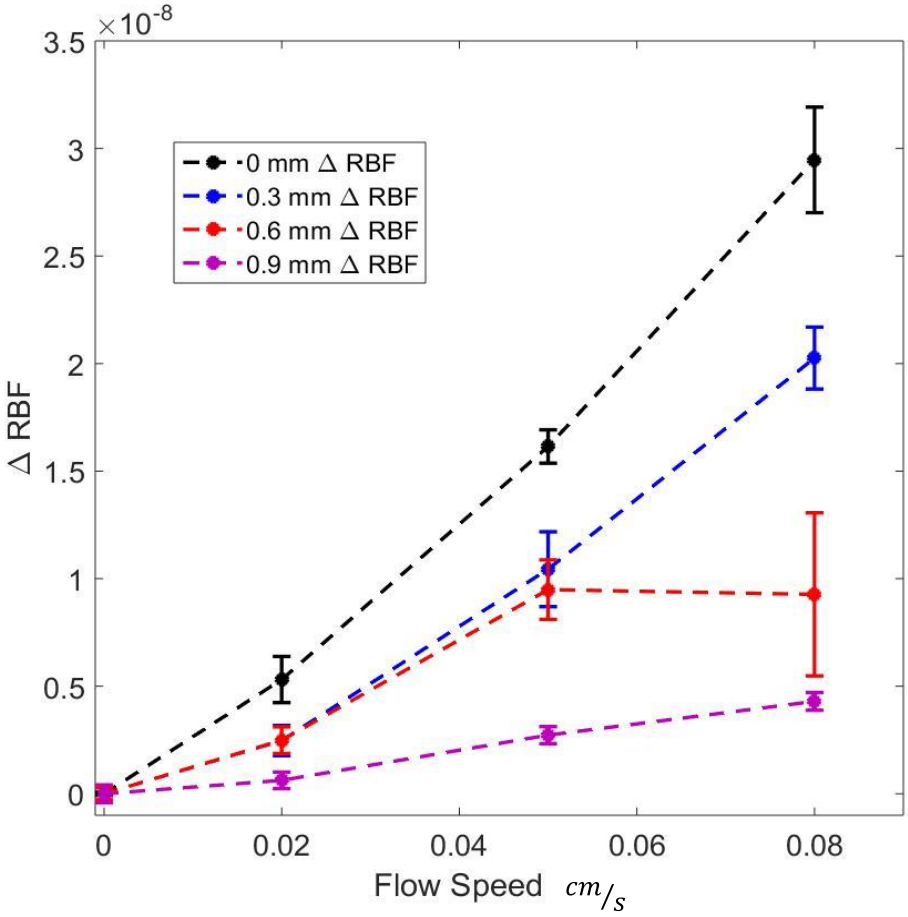

Figure 15: Relative change in DCS Brownian flow parameter for all four depths (dashed lines) as a function of flow speed.

The linearity in Figure 15 suggests that the syringe pump was operating near or at the set flow speed in addition to suggesting that the fitting used to extract the αD_B parameter was able to sense these changes in set flow speeds quite accurately. Additionally, from Figure 15 for depths of 0 mm and 0.9 mm flow channel submersion, distinguishability is distinct from depths of 0.3 and 0.6 mm, but these middle submersion depths are not significantly distinguishable from each other, disregarding the data point at 0.08 cm/s for a submersion depth of 0.6 mm. It is likely that experimental error, such as setting the pump at the incorrect flow speed for one of the scans, contributed to the large standard deviation at this point suggesting that this data point is inconclusive.

4.2.1 Defining a Sensitivity Parameter

A sensitivity parameter was then defined in order to quantify how the submersion depth of the flow channel altered the ability of DCS to distinguish between various flow speeds. Sensitivity was defined as $(\alpha D_{B(f,d)} - \alpha D_{B(0,d)})/\alpha D_{B(0,d)}$ where *f* corresponds to each flow speed (0, 0.02, 0.05, and 0.08 cm/s) and *d* references each depth (0, 3, 6, and 9 mm). Figure 16 shows the sensitivity parameter plotted as a function of depth. The four sets of bars represent each of the four depths and the bars themselves correspond to the appropriate sensitivity (i.e. navy bars represent the sensitivity of DCS between 0 and 0.02 cm/s).

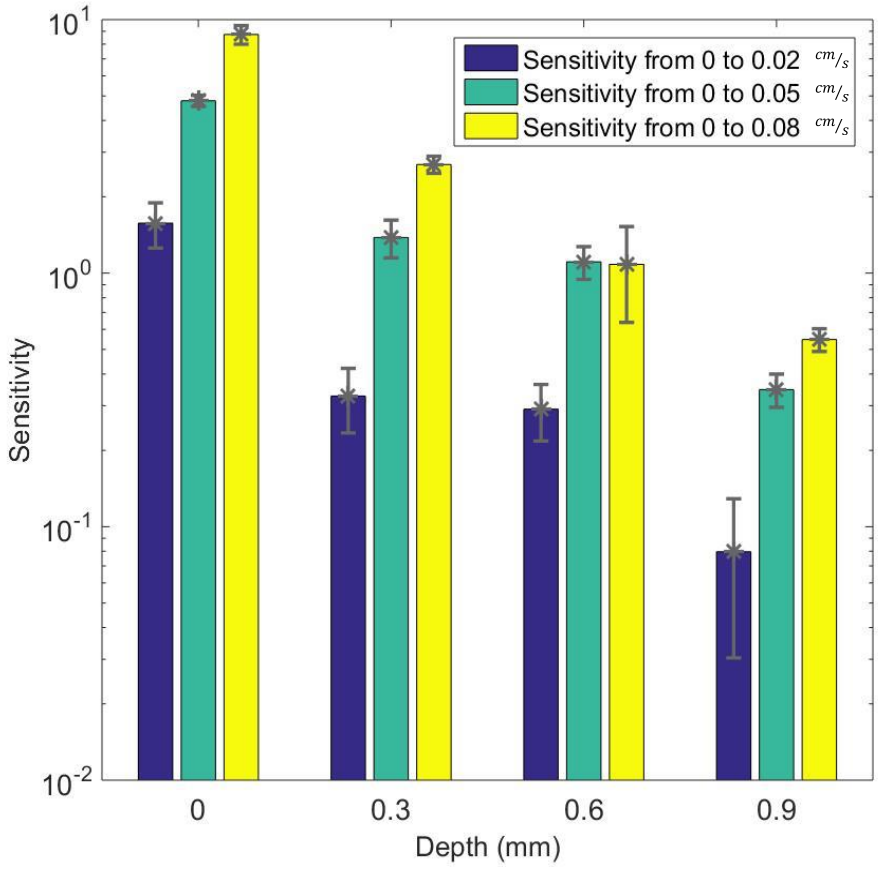

Figure 16: Sensitivity parameter, $(\alpha D_B(f,d) - (\alpha D_B(0,d))/ \alpha D_B(0,d)$, as a function of depth shown for three relative changes in flow parameter.

With increasing flow channel submersion depth, DCS sensitivity to relative changes in flow speed decreased. In addition, as shown in Figure 16, DCS sensitivity was highest between 0 and 0.08 cm/s (except for the 0.6 mm depth) and lowest between 0 to 0.02 cm/s. The mishap at depth 0.6 mm is likely due to experimental error, such as incorrect pump flow settings, that caused a large standard deviation, preventing conclusions to be drawn at that point. Overall, Figure 16

depicts the trends that ultimately validated the hypothesis DCS sensitivity decreases with increasing depth and increases with increasing difference in flow speed.

CHAPTER 5: A PRELIMINARY STUDY IN AN UNCONTROLLED SETTING

5.1 Purpose of Preliminary Study

The conclusions drawn from the experiments discussed in this thesis shed light on a preliminary study that was conducted in an uncontrolled setting. The goal of this preliminary study was to use readily available and low-cost alternatives to traditional scattering and absorbing particles to determine the feasibility of testing the effects of depth and varying surrounding optical properties of a flow channel on DCS sensitivity. The preliminary study was divided into two experimental tasks: 1) determination of depth sensitivity of DCS measurements and 2) examination of how optical properties of the surrounding media affect DCS measurements.

5.2 Experimental Setup

A saturated solution consisting of 4.2 g of Carnation milk powder dissolved in 12 mL deionized water (with an estimated reduced scattering coefficient of ~20 cm^{-1}) was made. The reduced scattering coefficient was calculated using Mie theory [53]. Parameters, such as the particle radius, were estimated to the best of the ability. The solution was loaded into a 2.2 cm-diameter syringe which was attached to a syringe pump at one end with a sink at the other end of the flow tubing.

The first task was to determine maximal depth sensitivity of the DCS system to distinguish between flow rates. The DCS probe was arranged in a manner so that the line between the source and detector fibers was perpendicular to the flow channel. The submersion of the tube in a scattering solution (1:4 dilution from the solution flowing through the tube) was increased by 0.5 mm until the distinguishing factors between static and flowing (volume flow rate of 6 mL/min) solution through the flow chamber tube disappeared. This volume flow rate was chosen to match a similar blood flow rate of a blood vessel with similar radius. By knowing the volume of the flow chamber, it was determined how much solution was required to raise the surface of the solution by 0.5 mm, increasing the depth of the flow channel with each addition.

The next task was to determine how varying the absorption and scattering properties of the surrounding medium impacted DCS sensitivity. Four liquid phantoms were made with varying concentrations of optical scatterers and absorbers as shown in Table 3.

Table 3: Target optical properties of surrounding medium for preliminary study.

Phantom ID	Description	Absorption Coefficient (cm^{-1})	Reduced Scattering Coefficient (cm^{-1})
P1	Low Scattering Low Absorbing	0.04	4
P2	Low Scattering High Absorbing	0.08	4
P3	High Scattering Low Absorbing	0.04	8
P4	High Scattering High Absorbing	0.08	8

The scattering solution directed through the flow channel was made by dissolving 4.2 grams of milk powder in 12 mL of deionized (DI) water. Subsequent dilutions of 1:2 and 1:4 were created corresponding to the high and low scattering liquid phantoms, respectively. Two additional solutions were made in order to create the optical phantoms. For the absorbing particles, red food dye (Betty Crocker gel food colors) was used. This was added each to the two scattering phantoms to create a total of four different phantoms: a low absorption phantom (1 drop of red food dye to the low and high scattering phantom) and a high absorption phantom (4 drops of red food dye were added to the low and high scattering phantom). In each of the four phantoms, the flow chamber was submerged 3 mm under the surface of the solution.

5.3 Preliminary Study Results

5.3.1 Depth Study Results

Figure 17 depicts the raw autocorrelation curves that resulted from the depth study when the flow channel submersion was varied but optical properties were held constant. The depth was increased subsequently by adding the appropriate volume of solution to increase the level of fluid in the chamber by 0.5 mm. Figure 17a shows DCS measurements taken with the pump off ("No Flow") and with a volume flow rate of 6 mL/min when the flow channel is just submerged in the surrounding solution. Figures 17b, 17c, and 17d depict the same DCS measurements at flow channel submersion depths of 0.5 mm, 1 mm, and 6 mm, respectively. DCS sensitivity between the no flow and flow measurements was lost at 3 mm flow channel submersion. Intermediate depths are not shown for concision.

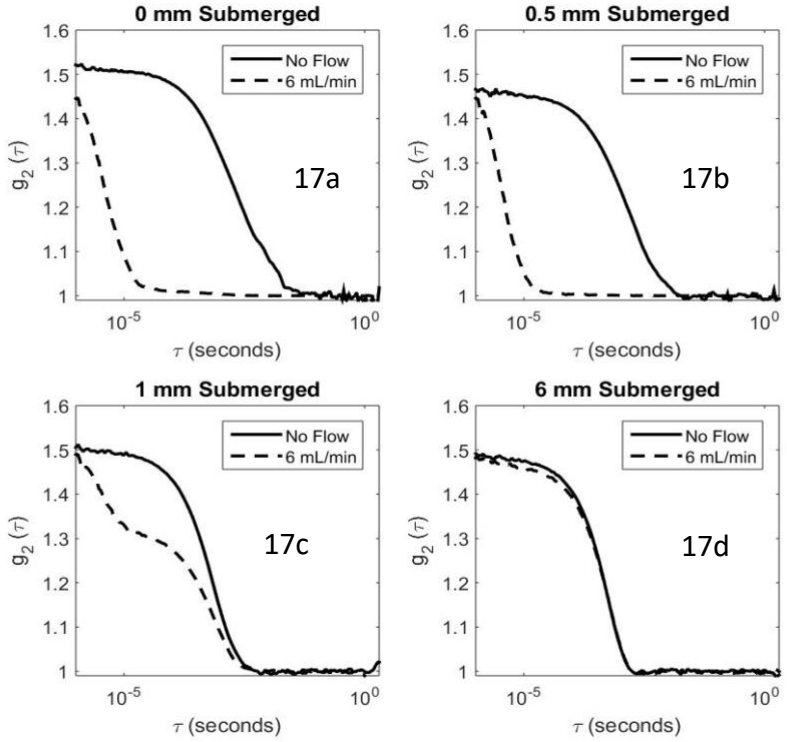

Figure 17: DCS measurements for both no flow and 6 mL/min at four flow channel submersion depths: 0, 0.5, 1.0, and 6.0 mm.

5.3.2 Varying the Optical Properties Study Results

Following the depth study, the second experimental task was to determine the effect of optical properties of the phantom have on DCS measurements. As shown in Figure 18, DCS measurements were taken with no flow and a volume flow rate of 6 mL/min through a flow channel submerged 3 mm in each of the four phantom solutions described in Table 3. Figure 18a depicts measurements from the low scattering and low absorbing phantom, Figure 18b was the low scattering and high absorbing, Figure 18c, the high scattering and low absorbing, while Figure 18d was the high scattering and high absorbing phantom. The following conclusions were drawn. When scatterer concentration was held constant at a low value (4 cm^{-1}), it was observed that the decay rate (or slope) of the autocorrelation curve increased with increasing absorber concentration. When scatterer concentration was held constant at a high value (8 cm^{-1}), the decay rate of the autocorrelation curve appears to decrease slightly with increasing absorber concentration. When absorber concentration was held constant at a low value (0.03 cm^{-1}), it is seen that the decay rate of the autocorrelation curve increased with increasing scatterer concentration. When absorber concentration was held constant at a high value (0.12 cm^{-1}), it was determined that the decay rate of the autocorrelation curve decreased with increasing scatterer concentration.

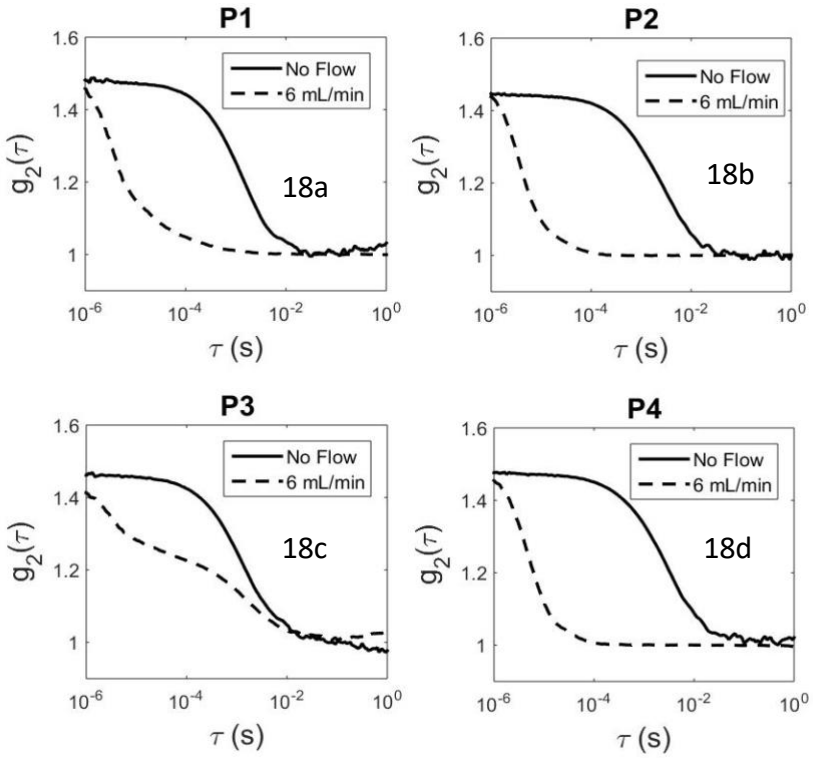

Figure 18: Phantom identification (i.e. P1, P2, P3, and P4) follows the assignment as presented in Table 3. DCS measurements for both no flow and 6 mL/min are shown for each phantom with the flow channel submerged 300 μm.

5.4 Preliminary Study Discussion

While little quantitative information was extracted from the preliminary study, at the time it was conducted, it provided enough convincing evidence to move forward and repeat these experiment in a more controlled manner. The preliminary study suggested that both the depth of the flow channel, the speed of the directed flow, and variations in optical properties of the surrounding media all affected the decay rates of the resulting autocorrelation curves. The preliminary study also demonstrated the importance of having controlled experimental parameters and well-known optical properties in order to accurately derive relative changes in flow rates from DCS measurements. Without these parameters, deriving such sensitivity metrics and flow indices becomes a difficult task.

CHAPTER 5: CONCLUSIONS

The experiments presented in this thesis have validated the ability of the DCS setup to collect meaningful and reproducible data. The data presented here demonstrates how DCS sensitivity to distinguish between flow rates is affected by 1) the depth of the flow channel and 2) the variation in optical properties of the solution that is surrounding the submerged flow channel. It is important to note that all experiments conducted for this thesis were conducted using a DCS probe that has a source-detector separation of 1.5 mm. This degree of separation is below the threshold for operating in the diffusive regime. Therefore, diffusion theory is no longer valid. Though, diffusion theory can still be used to fit the experimental data, but will result in faulty output parameters for the optical scattering and absorbing coefficients that do not match the experimental conditions. While this was not problematic in these experiments as the goal was to determine *relative* changes between flow rates/speeds, this would become an issue if one were aiming to determine the absolute flow velocity from the DCS measurements.

It is thought that implementation of the Monte Carlo simulation could help alleviate the issues that arise with using short source-detector separations in DCS. In brief, the Monte Carlo method consists of a series of computational algorithms that uses the principles of randomness and probability to determine a numerical outcome to a problem. Here, the Monte Carlo method devised by my advisor, Dr. Karthik Vishwanath, was utilized to construct an autocorrelation curve based on a given set of experimental values (μ_s', μ_a, ρ, etc.). The idea was the following; if a set of experiments was conducted with a known set of experimental parameters, same experimental parameters into the Monte Carlo simulation and compare the results of the simulated autocorrelation curves to those from the experiment. In essence, while diffusion theory is not valid when using short source-detector separations, Monte Carlo simulations may provide a method of bypassing the issues with short source-detector probes being outside of the diffusion theory range. It is thought that one could fit the experimental data with the Monte Carlo simulation and derive relative experimental parameters from there.

CHAPTER 6: FUTURE WORK

In regard to future work to continue this research on diffuse correlation spectroscopy, there are many possibilities that I wish I would have gotten the chance to explore. I am hoping that by sharing ideas here, students that come through the lab and work on this project will be inspired to pursue some of the outlets discussed or use these ideas to develop pathways of their own.

6.1 Compressing the DCS system

Considering that my thesis work has validated the applicability of our DCS system and its ability to reliably and reproducibly sense relative changes in flow with tissue-simulating optical phantoms, I would very much like the next steps include the implementation of this instrument in a real biological tissue sample. While currently the only way to take measurements on a human study participant is to bring them into our lab, I believe it is feasible to compress our DCS system (laser, fiber optic probe, APD, and correlator) into one compact apparatus that can easily be transported to alternate locations. This would allow for many opportunities for us to collaborate with researchers in other departments across our campus and other campuses in addition to presenting the possibility of integrating our DCS system into a clinic.

6.2 Monitoring the Blanch Response for Early Indication of Pressure Ulcers

Pressure ulcers, or more commonly known as bed sores, affect many bedridden and stationary patients in hospitals and healthcare facilities. Pressure ulcers are the death of tissue due to constant pressure or compression of a certain region of tissue, especially when boney prominences are present as well, such as near the tailbone and elbows. Currently, the gold standard to determine a pressure ulcer is to push on the affected area with one or a few fingers and release, monitoring the color change that occurs. With healthy skin, the induced pressure from the fingers will push blood out of the tissue, causing the tissue to look white (or “blanch”) when the pressure is released. When a pressure ulcer is forming, or already formed, this blanch response becomes increasing absent even as external manipulation of pressure is applied. The blanch response is a highly subjective test as there are no documented directives in how to conduct such a test. With this in mind, I propose using DCS as a method of early monitoring of pressure ulcer formation. As tissue dies, it will experience a loos of blood flow and considering DCS has relative flow sensing capabilities, it serves as a promising alternative to pressure ulcer monitoring. This would allow for a quantitative measure of bed sore progression as opposed to the solely subjective blanch response testing that exists today.

6.3 The Integration of DCS Probes into the Functional Near-Infrared Spectroscopy (fNIRS) System

With our collaborators in the psychology department, there is an excellent study being conducted on the hemodynamic alterations that occur in the brain when stress is induced.

Currently, the head cap used to collect the data is comprised of many fNIRS probes that allow for the determination of concentrations of oxy- and deoxy-hemoglobin. This determination allows for the researchers to determine whether or not metabolic demand to that region of the brain was increased, decreased, or relatively constant which in turns relays information regarding brain activation. Integrating the DCS system into this head cap would allow for the determination of which areas of the brain are not only undergoing changes in oxy- and deoxy-hemoglobin concentrations, but also which areas of the brain are experiencing changes in relative flow.

6.4 DCS on Solid Phantoms

In addition to utilizing our DCS system to collect data on human study participants or animal models, I would like to test the DCS system on a series of solid phantoms with flow channels embedded within. This would provide another perspective to how the DCS sensitivity changes with depth and varying optical properties of the medium surrounding a flow channel. It would be interesting to investigate how DCS sensitivity compares when measurements are taken at the same depth for a liquid phantom and a solid phantom with identical physical properties. While solid optical phantoms may make the experimental data collection less tedious than working with solutions, solid phantoms do pose a number of issues that would have to be well thought out before implementing. For example, the construction of optical phantoms is much more difficult than one may expect. It is critical that one ensures the uniformity of the optical properties throughout the entire solid phantom so that the DCS measurements are valid. This requires not only special machinery, but also a great deal of time and precision. Since we are limited on time and equipment, it would be wise to look for a potential collaboration in a related field. I am aware of some groups in which their main goal is to construct solid optical phantoms for similar testing to which we are aiming to conduct. Another issue that arises is that if the goal is to measure how depth of submersion affects DCS sensitivity, one cannot change the depth of a flow channel embedded in a solid optical phantom. It may be best to instead stack solid phantoms of identical optical properties to achieve the desired submersion depth.

Whether a theorist or an experimentalist, the potential pathways to explore when conducting research using DCS are endless. I hope that my ideas for future work inspire new ideas that further the research in a subject that has immense clinical potential. While my focus was strictly medical related due to my own personal interests, DCS does not have to be restricted to healthcare. Flow is everywhere and I am excited to see the future of DCS as a sensing instrument implementing in a variety of research areas.

APPENDIX I: TIPS FOR OPTIMIZING THE DCS SYSTEM

The DCS setup is relatively straight forward and user-friendly. The tabletop setup consists of the DCS laser, a series of three mirrors focusing this laser light through a lens and into the single mode fiber probe, an APD, and lastly, the correlator board. Even with everything bolted down to the table, the DCS system is extremely sensitive to movement. It is important to optimize the DCS set up before each set of measurements is conducted. The following are suggested:

- Check the power output at the detector end of the fiber probe. For most experiments, a power of approximated 40-50 mW is typically sufficient. Note that the wavelength on the power meter must be set to the wavelength of the laser source in use for accurate readings. Record this power in a lab notebook. If the power is not sufficient, appropriate alignment to the DCS setup is highly encouraged.
- Depending on the probe's source-detector separation, it is important to record the photon count that is found on the LSI interface. For short source-detector separations, such as 0.5 or 1.5 mm, these counts are typically 200-400 kHz on the phantom block and your finger, which is sufficient to get quality DCS curves that are considered to be void of any ambient light. For larger probes, such as the one containing the 5 and 10 mm source-detector fiber separations, photon counts will be much lower, typically between 30-40 kHz on both the phantom block and your finger. Photon counts lower than 10-20 kHz will not usually be sufficient to produce decorrelation.
- Ensure data is collected in a dark room. Computer light is ok but the overhead light will create noise in DCS measurements.
- Collect the following reference measurements at the beginning of each experiment: a DCS measurement on the phantom block, a DCS measurement on a white sheet of paper, a DCS measurement on the sample you are testing when there is no flow and no perturbations to the sample. This will serve as a baseline.

APPENDIX II: USING THE DCS LSI SOFTWARE & MATLAB® INTERFACE

The DCS software is easy to use but I will provide a list of direct steps of how to collect a sample measurement and load it into MATLAB® for analysis. My hope is that these simplified directions will help new students get the hang of things more quickly.

1. Plug the LSI correlator into your computer with the USB cord provided.
2. Plug the LSI correlator into a power source. You will see the white light on the front turn on indicating the hardware is powered on.
3. Initiate the LSI correlator software on your computer. This must be done after the LSI correlator hardware is powered on.
4. Set the appropriate time for the software to collet DCS measurements, usually this is 5 seconds, but is free to vary.
5. Take sample DCS measurement with fiber probe on solid phantom block. Check the photon count and ensure that it is sufficient (as discussed above; see Appendix I).
6. Save your measurement that you just took.
7. Initiate another measurement on your sample. Take a minimum of three repeat scans, five is better. Save each in a manner that is clear. Note this notation in your lab notebook. "Scan1" may seem reasonable at the time but you will not remember what this was when you go to write your thesis or capstone paper months or years later.
8. Load the data to MATLAB®.
    a. Open MATLAB®.
    b. Set your path to "C:\Users\osimlab-dcs\Desktop" as this is where the function is that will load your data you saved from the autocorrelator software.
    c. Name your variable appropriately and call the "autocor_DCS" function (see example in screen grab below).

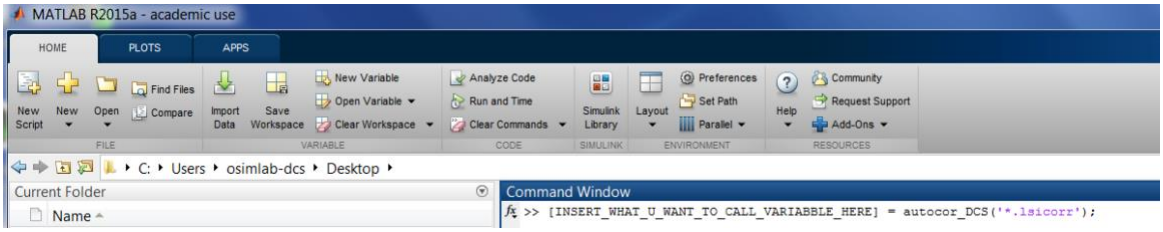

    d. Press enter.
    e. Search for your file in the folder that you saved it to when saving from the LSI software interface.
    f. Select your file and press enter.
    g. Your variable (as an autocorrelation curve) will now be in your workspace (1 x 310 double) as well as "t" which should be a 310 x 1 double. This is your time scale and x-axis.

h. Plot this to verify the shape you should expect. Do this by initiating a semilog plot with respect to the x-axis. Ex: "semilogx(t, 1+what_you_named_your_variable). A plot with an autocorrelation curve should open in a new window.
i. Let the data analysis begin! Note: *For larger data sets, it is more efficient to set up structures within MATLAB® to analyze. Dr. Vishwanath will be an excellent reference on how to create and manipulate structures.*

REFERENCES

1. Chylek, P., *Light-Scattering by Small Particles in an Absorbing Medium.* Journal of the Optical Society of America, 1977. **67**(4): p. 561-563.
2. Meehan, E.J., *Light Absorption and Scattering in Colloidal Suspensions of Strongly Absorbing Substances.* Journal of Colloid and Interface Science, 1968. **27**(3): p. 388
3. Anderson, N.M. and P. Sekelj, *Light-Absorbing and Scattering Properties of Non-Haemolysed Blood.* Physics in Medicine and Biology, 1967. **12**(2): p. 170-&.
4. Yu, G., *Near-infrared diffuse correlation spectroscopy in cancer diagnosis and therapy monitoring.* J Biomed Opt, 2012. **17**(1): p. 010901.
5. Pine, D.J., et al., *Diffusing wave spectroscopy.* Phys Rev Lett, 1988. **60**(12): p. 1134-1137.
6. MacKintosh, F.C. and S. John, *Diffusing-wave spectroscopy and multiple scattering of light in correlated random media.* Phys Rev B Condens Matter, 1989. **40**(4): p. 2383-2406.
7. Weitz, D.A., et al., *Nondiffusive Brownian motion studied by diffusing-wave spectroscopy.* Phys Rev Lett, 1989. **63**(16): p. 1747-1750.
8. Boas, D.A., *Diffuse photon probes of structural and dynamical properties of turbid media : theory and biomedical applications*. 1996, Graduate School of Arts and Sciences, University of Pennsylvania.
9. Yu, G., et al., *Hemodynamic measurements in rat brain and human muscle using diffuse near-infrared absorption and correlation spectroscopies.* Optical Tomography and Spectroscopy of Tissue V, 2003. **4955**: p. 164-174.
10. Gagnon, L., et al., *Double layer estimation of flow changes using diffuse correlation spectroscopy.* Optical Tomography and Spectroscopy of Tissue Viii, 2009. **7174**.
11. Liang, J.M., et al., *A Study on Blood Flow Measurement by Diffuse Correlation Spectroscopy.* Spectroscopy and Spectral Analysis, 2012. **32**(10): p. 2749-2752.
12. Lin, Y., et al., *Noncontact diffuse correlation spectroscopy for noninvasive deep tissue blood flow measurement.* Journal of Biomedical Optics, 2012. **17**(1).
13. Yu, G.Q., *Diffuse Correlation Spectroscopy (DCS): A Diagnostic Tool for Assessing Tissue Blood Flow in Vascular-Related Diseases and Therapies.* Current Medical Imaging Reviews, 2012. **8**(3): p. 194-210.
14. Durduran, T. and A.G. Yodh, *Diffuse correlation spectroscopy for non-invasive, micro-vascular cerebral blood flow measurement.* Neuroimage, 2014. **85**: p. 51-63.
15. Selb, J., et al., *Sensitivity of near-infrared spectroscopy and diffuse correlation spectroscopy to brain hemodynamics: simulations and experimental findings during hypercapnia.* Neurophotonics, 2014. **1**(1).
16. Selb, J., et al., *Feasibility of Diffuse Correlation Spectroscopy for Prolonged Monitoring of Cerebral Autoregulation during Neurocritical Care.* Journal of Cerebral Blood Flow and Metabolism, 2016. **36**: p. 728-729.
17. Rosenberry, R., et al., *Measurement of Skeletal Muscle Blood Flow with Near-infrared Diffuse Correlation Spectroscopy.* Faseb Journal, 2017. **31**.
18. Meinke, M., et al., *Empirical model functions to calculate hematocrit-dependent optical properties of human blood.* Appl Opt, 2007. **46**(10): p. 1742-53.

19. Dougherty, R.L., et al., *Correlation Transfer - Development and Application.* Journal of Quantitative Spectroscopy & Radiative Transfer, 1994. **52**(6): p. 713-727.
20. Osborn, R.K. and E.H. Klevans, *Photon Transport Theory.* Annals of Physics, 1961. **15**(2): p. 105-140.
21. Ackerson, B.J., et al., *Correlation Transfer - Application of Radiative-Transfer Solution Methods to Photon-Correlation Problems.* Journal of Thermophysics and Heat Transfer, 1992. **6**(4): p. 577-588.
22. Jacques, S.L., *Optical properties of biological tissues: a review.* Phys Med Biol, 2013. **58**(11): p. R37-61.
23. Haskell, R.C., et al., *Boundary-Conditions for the Diffusion Equation in Radiative-Transfer.* Biophysical Journal, 1994. **66**(2): p. A378-A378.
24. Boas, D.A., et al., *Establishing the diffuse correlation spectroscopy signal relationship with blood flow.* Neurophotonics, 2016. **3**(3).
25. Boas, D.A. and A.G. Yodh, *Spatially varying dynamical properties of turbid media probed with diffusing temporal light correlation.* Journal of the Optical Society of America a-Optics Image Science and Vision, 1997. **14**(1): p. 192-215.
26. Irwin, D., et al., *Influences of tissue absorption and scattering on diffuse correlation spectroscopy blood flow measurements.* Biomed Opt Express, 2011. **2**(7): p. 1969-85.
27. Boas, D.A., et al., *Establishing the diffuse correlation spectroscopy signal relationship with blood flow.* Neurophotonics, 2016. **3**(3): p. 031412.
28. Carp, S.A., et al., *Due to intravascular multiple sequential scattering, Diffuse Correlation Spectroscopy of tissue primarily measures relative red blood cell motion within vessels.* Biomed Opt Express, 2011. **2**(7): p. 2047-54.
29. Verdecchia, K., et al., *Assessment of the best flow model to characterize diffuse correlation spectroscopy data acquired directly on the brain.* Biomed Opt Express, 2015. **6**(11): p. 4288-301.
30. Vishwanath, K. and Zanfardino, S. (2017). *In Situ Optical Tissue Diagnostics/Laser Speckle-Based Spectroscopy Techniques in Biomedicine*. Encyclopedia of Moden Optics Second Edition. p. 95-99.
31. Cheng, R., et al., *Noninvasive quantification of postocclusive reactive hyperemia in mouse thigh muscle by near-infrared diffuse correlation spectroscopy.* Applied Optics, 2013. **52**(30): p. 7324-7330.
32. Buckley, E., et al., *Cerebral hemodynamics of preterm infants during postural intervention measured with diffuse correlation spectroscopy and transcranial doppler ultrasound.* Journal of Cerebral Blood Flow and Metabolism, 2009. **29**: p. S470-S471.
33. Gagnon, L., et al., *Investigation of diffuse correlation spectroscopy in multi-layered media including the human head.* Optics Express, 2008. **16**(20): p. 15514-15530.
34. Durduran, T., et al., *Validation of diffuse correlation spectroscopy for non-invasive, continuous monitoring of CBF in neonates with congenital heart defects.* Annals of Neurology, 2008. **64**: p. S63-S63.
35. Yu, G., et al., *Validation of diffuse correlation spectroscopy for muscle blood flow with concurrent arterial spin labeled perfusion MRI.* Opt Express, 2007. **15**(3): p. 1064-75.
36. Buckley, E.M., et al., *Decreased microvascular cerebral blood flow assessed by diffuse correlation spectroscopy after repetitive concussions in mice.* J Cereb Blood Flow Metab, 2015. **35**(12): p. 1995-2000.

37. Weingarten, M.S., et al., *Diffuse Correlation Spectroscopy Monitoring of Capillary Flow as It Correlates to Segmental Pressures and Vascular Disease.* Wound Repair and Regeneration, 2014. **22**(2): p. A65-A65.
38. Liu, Q., et al., *Laser speckle contrast imaging: monitoring blood flow dynamics and vascular structure of photodynamic therapy.* Optics in Health Care and Biomedical Optics: Diagnostics and Treatment Ii , Pts 1 and 2, 2005. **5630**: p. 26-33.
39. Briers, J.D. and X.W. He, *Laser speckle contrast analysis (LASCA) for blood flow visualization: improved image processing.* Optical Diagnostics of Biological Fluids Iii, Proceedings Of, 1998. **3252**: p. 26-33.
40. Yazdanfar, S., et al., *Diagnostic blood flow monitoring during therapeutic interventions using color Doppler optical coherence tomography.* Coherence Domain Optical Methods in Biomedical Science and Clinical Applications Ii, Proceedings Of, 1998. **3251**: p. 126-132.
41. Wong, R.C.K., et al., *The visualization of submucosal blood vessels by color Doppler flow imaging using Optical Coherence Tomography: Potential use in peptic ulcer hemorrhage.* Gastrointestinal Endoscopy, 1997. **45**(4): p. 74-74.
42. Buckley, E.M., et al., *Cerebral hemodynamics in preterm infants during positional intervention measured with diffuse correlation spectroscopy and transcranial Doppler ultrasound.* Opt Express, 2009. **17**(15): p. 12571-81.
43. Yazdi, H.S., et al., *Mapping breast cancer blood flow index, composition, and metabolism in a human subject using combined diffuse optical spectroscopic imaging and diffuse correlation spectroscopy.* Journal of Biomedical Optics, 2017. **22**(4).
44. Carp, S.A., et al., *Validation of diffuse correlation spectroscopy measurements of rodent cerebral blood flow with simultaneous arterial spin labeling MRI; towards MRI-optical continuous cerebral metabolic monitoring.* Biomed Opt Express, 2010. **1**(2): p. 553-565.
45. Durduran, T., et al., *Diffuse optics for tissue monitoring and tomography.* Reports on Progress in Physics, 2010. **73**(7).
46. Liang, J.M., et al., *[A study on blood flow measurement by diffuse correlation spectroscopy].* Guang Pu Xue Yu Guang Pu Fen Xi, 2012. **32**(10): p. 2749-52.
47. Farzam, P. and T. Durduran, *Multidistance diffuse correlation spectroscopy for simultaneous estimation of blood flow index and optical properties.* Journal of Biomedical Optics, 2015. **20**(5).
48. Cortese, L., et al., *Liquid phantoms for near-infrared and diffuse correlation spectroscopies with tunable optical and dynamic properties.* Biomedical Optics Express, 2018. **9**(5): p. 2068-2080.
49. Vishwanath, K. and M.A. Mycek, *Polystyrene microspheres in tissue-simulating phantoms can collisionally quench fluorescence.* Journal of Fluorescence, 2003. **13**(1): p. 105-108.
50. Taroni, P., et al., *In vivo absorption and scattering spectroscopy of biological tissues.* Photochemical & Photobiological Sciences, 2003. **2**(2): p. 124-129.
51. Ivanov, K.P., M.K. Kalinina, and Y.I. Levkovich, *Blood flow velocity in capillaries of brain and muscles and its physiological significance.* Microvascular Research, 1981. **22**(2): p. 143-155.
52. Beddard, G.S., et al., *Fluorescence Decay Kinetics of Invivo Chlorophyll Measured Using Low Intensity Excitation.* Biochimica Et Biophysica Acta, 1979. **545**(1): p. 165-174.

53. Wang, L.V. and H.-I. Wu, *Raleigh theory and Mie theory for single scatterer*, in *Biomedical opticsl priniciples and imaging*. 2007, John Wiley & Sons: Hobken, NJ.